

Spin Dynamics in the van der Waals Ferromagnet CrTe₂ Engineered by Nb Doping

Dhan Raj Lawati,^{1†} Prem Bahadur Karki,^{2†} Jitender Kumar,^{1†} Karishma Prasad,^{3†} Mohamed A. Elekhtiar,⁴ Kai Huang,⁴ Bibek Tiwari,⁴ Suvechhya Lamichhane,⁴ Rupak Timalisina,¹ Zane Hubble,² Ayodimeji E. Aregbesola,² John Watt,⁵ Sy-Hwang Liou,⁴ Evgeny Y. Tsymbal,⁴ Jian Wang,^{3} Kapildeb Ambal,^{2*} and Abdelghani Laraoui^{1,4*}*

¹ Department of Mechanical & Materials Engineering, University of Nebraska-Lincoln, Lincoln, NE 68588, United States

² Department of Mathematics, Statistics, and Physics, Wichita State University, Wichita, KS 67260, United States

³ Department of Chemistry and Biochemistry, Wichita State University, Wichita, KS 67260, United States

⁴ Department of Physics and Astronomy and Nebraska Center for Materials and Nanoscience, University of Nebraska-Lincoln, Lincoln, NE 68588, United States

⁵ Center for Integrated Nanotechnologies, Los Alamos National Laboratory, Los Alamos, NM, 87545 United States

*Corresponding Authors: alaraoui2@unl.edu, kapildeb.ambal@wichita.edu, and jian.wang@wichita.edu

[†]Equal contribution

Abstract

Understanding and controlling spin dynamics in two-dimensional (2D) van der Waals (vdW) ferromagnets is essential for their application in magnonics and hybrid quantum platforms. Here, we investigate the spin dynamics of the vdW ferromagnet 1T-CrTe₂ and demonstrate their systematic tunability via niobium (Nb) substitution in Cr_{1-x}Nb_xTe₂ ($x = 0 - 0.2$). Ferromagnetic resonance (FMR) spectroscopy reveals that Nb doping enables wide-band tuning of the resonance frequency from 40 GHz down to the few-GHz regime, accompanied by a moderate increase in the Gilbert damping constant from ~ 0.066 to ~ 0.14 , while preserving robust room-temperature ferromagnetism. Complementary magnetometry shows a concurrent reduction of the Curie temperature and saturation magnetization with increasing Nb content. Density functional theory calculations attribute the observed spin-dynamic trends to Nb-induced modifications of magnetic anisotropy and magnetic exchange interactions. Furthermore, CrTe₂ flakes (~ 100 nm thick) exhibit lower resonance frequencies than bulk crystals, consistent with thickness-dependent magnetic anisotropy. These results establish Nb-doped CrTe₂ as a tunable vdW ferromagnet with controllable spin dynamics, extending its functionality from spintronics to broadband magnonics and quantum magnonics.

1. Introduction

Emerging two-dimensional (2D) van der Waals (vdW) magnets^[1,2] provide a versatile platform for exploring and engineering magnetism beyond the limits of conventional bulk materials. Reduced dimensionality enables unprecedented control of magnetic properties through layer-by-layer engineering,^[3-5] twisting,^[6] doping,^[7-9] and proximity effects.^[10-12] Moreover, vdW magnets can be integrated into heterostructures with other vdW materials enabling electrical, mechanical, and optical control of magnetism.^[2,13,14] Their weak interlayer bonding permits easy transfer onto functional substrates such as diamond or hexagonal boron nitride (hBN). These materials host optically addressable spin qubits, such as nitrogen-vacancy (NV) centers in diamond and defect-

based spin centers in hBN, providing long coherence times and enabling strong proximity coupling for nanoscale sensing and hybrid quantum systems.^[15–20]

Despite intense research activity since the initial discovery of 2D magnetism in 2017,^[3,4] the spin dynamics of vdW magnets, central to magnonics, remain poorly understood or largely unexplored in many newly discovered materials. To date, spin-wave (SW)/magnon modes have been observed in only limited number of vdW systems, such as CrI₃,^[21,22] CrCl₃,^[23] FePS₃,^[24] MnBi₂Te₄,^[25] CrSBr,^[26] and α -RuCl₃.^[27] Recent electrical detection of spin pumping experiments in Cr₂Ge₂Te₆/Pt flakes showed GHz magnetization dynamics with a low magnetic damping $\sim 0.4 - 1 \times 10^{-3}$.^[28] Establishing broadly tunable spin-dynamic properties in vdW magnets therefore remains an important open challenge for magnonics applications.^[29,30]

CrTe₂, a member of the transition-metal dichalcogenide (TMD) family, is a particularly promising candidate owing to its robust ferromagnetism and structural versatility. It crystallizes in several structural polymorphs including *1H*, *2H*, *1T_d*, and *1T* phases.^[31] Notably, the *1T* phase of CrTe₂ exhibits ferromagnetism with a Curie temperature (T_C) above room temperature in bulk crystals,^[32] exfoliated thin flakes,^[20,33] and epitaxially grown monolayers.^[34,35] While most thick (> 10 nm) CrTe₂ crystals and flakes^[32,33] display in-plane magnetic anisotropy, few-monolayer epitaxial films exhibit strong perpendicular magnetic anisotropy,^[34,35] highlighting CrTe₂ as a versatile vdW ferromagnet for spintronic applications.^[14,36,37] Recent multiscale modeling showed that interfacing CrTe₂ layer with various Te-based layers enabled the control of the magnetic exchange and Dzyaloshinskii-Moriya interactions,^[38] relevant to topological spin textures.^[39–42] However, despite these advances, the spin dynamics and magnonic properties of CrTe₂ have remained largely unexplored.

Here, we explore and engineer spin dynamics in the vdW ferromagnet *1T*-CrTe₂ by investigating its dynamic magnetic response using ferromagnetic resonance (FMR) spectroscopy at room temperature. To achieve systematic and controllable tunability of these spin-dynamic properties without suppressing robust room-temperature ferromagnetism, we employ niobium (Nb) substitution in Cr_{1-x}Nb_xTe₂ ($x = 0 - 0.2$) crystals grown by indirect synthesis. Nb doping provides a chemically stable and scalable route to modify magnetic interactions, thereby enabling control of spin dynamics. Structural characterization confirms high crystalline quality and Nb incorporation, while magnetometry shows that all doped crystals remain ferromagnetic, with Curie temperature decreasing modestly from ~ 315 to ~ 300 K and the saturation magnetization reduced with increasing Nb content. FMR measurements reveal that Nb doping enables wide-band tuning of spin dynamics, yielding a progressive reduction of the resonance frequency and a moderate increase of the Gilbert damping constant α from ~ 0.066 to ~ 0.14 . Density functional theory (DFT) calculations attribute these trends to Nb-induced modifications of magnetic anisotropy, spin-orbit coupling, and exchange coupling. Lower (a few GHz) ferromagnetic resonance frequencies of ~ 100 -nm -thick CrTe₂ flakes compared to bulk crystals are explained by thickness-dependent magnetic anisotropy.^[35] Together, these results establish Nb-doped CrTe₂ as a vdW ferromagnet with widely tunable spin dynamics, extending its applicability to magnon spintronics,^[43,44] topological magnonics,^[45,46] and quantum magnonics.^[47–51]

2. Results and Discussion

2.1. Crystal Growth and Structural Characterization

1T-Cr_{1-x}Nb_xTe₂ ($x = 0, 0.05, 0.10, 0.15, 0.20$) crystals were prepared via oxidation of their respective precursors KCr_{1-x}Nb_xTe₂ ($x = 0.05 - 0.2$). The precursors were synthesized by direct

solid-state reaction^[52] of the constituent elements (see Experimental Section and Figure S1.1, Supporting Information). X ray diffraction (XRD) measurements were performed on $\text{Cr}_{1-x}\text{Nb}_x\text{Te}_2$ ($x = 0, 0.05, 0.10, 0.15, 0.20$), see Supporting Information S1.2 and Figure S1.2. The lattice parameter ($a=b$) of the parent pristine CrTe_2 crystal is 3.7803 Å and decreases to 3.7761 Å with Nb doping up to 20%. A monotonic shift of the Bragg peak towards lower angles with increasing the Nb concentration is observed (Figure S1.2b, Supporting Information), indicating a lattice contraction in the ab plane (see Figure 6a) due to the incorporation of Nb into the CrTe_2 lattice. An increase in the c/a ratio (Figure S1.2c, Supporting Information) with increasing the Nb concentration further confirms the lattice expansion along the crystallographic c axis. Such contraction/expansion of the unit cell have been observed upon replacing Cr with vanadium (V) in the first report of ferromagnetism in CrTe_2 crystals.^[32] Changes in the lattice parameters have a clear impact on the magnetic and electrical properties of CrTe_2 .^[32] For instance, a reduction in the magnetic moment by 60% in the room-temperature electrical conductivity was observed in 2% V-doped CrTe_2 , which is attributed to the onset of antiferromagnetic (AFM) coupling.^[32] Several studies have further indicated that the stabilization of ferromagnetic or AFM ground states in CrTe_2 is strongly correlated with the lattice parameters.^[53,54] Theoretical calculations revealed that the ground state of a monolayer is Z-type AFM, associated with a reduction of the in-plane lattice constant from ~ 3.8 Å in the bulk to ~ 3.57 Å in the monolayer.^[53,54] The XRD and DFT calculation (Section 2.4) results corroborate with our bulk magnetic properties of the $\text{Cr}_{1-x}\text{Nb}_x\text{Te}_2$ crystals, discussed in detail in Section 2.2.

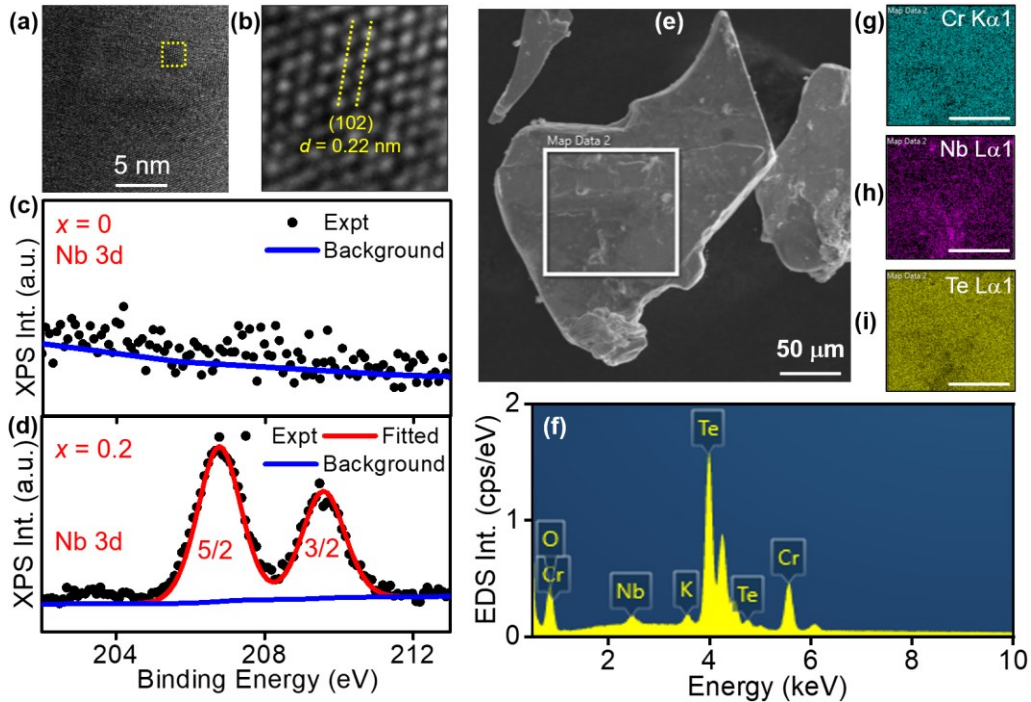


Figure 1. (a) HRTEM image of 1T- $\text{Cr}_{0.8}\text{Nb}_{0.2}\text{Te}_2$ flake, showing different crystal orientations. (b) Zoomed section of HRTEM image in (a) showing the (102) plane. High Resolution XPS spectra of CrTe_2 (c) and $\text{Cr}_{0.8}\text{Nb}_{0.2}\text{Te}_2$ (d) crystals. The scattered curves are measured XPS curves while the solid red lines are fits. The Blue line shows the background coming from inelastic scattered electrons. (e) SEM image of a selected $\text{Cr}_{0.8}\text{Nb}_{0.2}\text{Te}_2$ micro-crystal. (f) SEM-EDS spectrum showing the presence of Cr, Nb, Te in addition to O due to oxidation of the surface and K, a residue from the sample preparation. SEM-EDS element maps of Cr $\text{K}\alpha 1$ (g), Nb $\text{L}\alpha 1$ (h), and Te $\text{L}\alpha 1$ (i), respectively, highlighted by a solid square in (e).

Selected $\text{Cr}_{1-x}\text{Nb}_x\text{Te}_2$ ($x = 0 - 0.2$) crystals were further characterized using high-resolution transmission electron microscopy (HRTEM). Figure 1a and Figure S1.3.1 (Supporting information) show HRTEM images of different $\text{Cr}_{0.8}\text{Nb}_{0.2}\text{Te}_2$ flakes, obtained by grinding large crystals, confirming their polycrystalline nature, consistent with the XRD peaks in Figure S1.2a in the Supporting Information. Zoomed HRTEM images of Flake 1 in Figure 1b and Flake 2 in Figure S1.3.2b show lattice spacing d of ~ 0.22 nm and ~ 0.32 nm consistent with the $\{102\}$ and $\{100\}$ interplanar spacings, corroborating the XRD results.

To further check the presence of Nb, X-ray photoelectron spectroscopy (XPS) and energy-dispersive X-ray spectroscopy (EDS) measurements were conducted on selected $\text{Cr}_{1-x}\text{Nb}_x\text{Te}_2$ crystals. As expected, no Nb was detected in pristine CrTe_2 crystals in the XPS spectra (Figure 1c). However, for $\text{Cr}_{0.8}\text{Nb}_{0.2}\text{Te}_2$ crystal (Figure 1d), there are two measured peaks (filled circles) at binding energies of ~ 206.78 eV and ~ 209.58 eV, corresponding to Nb $3d_{5/2}$ and $3d_{3/2}$ electronic states, respectively.^[55] The measured peaks in Figure 1d were fitted (solid lines) using a combined Lorentzian and Gaussian functions.^[56,44] XPS peaks of Te and Cr were obtained in both pristine and $\text{Cr}_{0.8}\text{Nb}_{0.2}\text{Te}_2$ crystals (see Figure S1.4, Supporting Information) with binding energies of ~ 572.5 (582.8) eV for Te $3d_{5/2}$ ($3d_{3/2}$) doublets, and ~ 575.8 (586.4) eV, for Cr $2p_{3/2}$ ($3p_{1/2}$) doublets, respectively.^[35] Although the Nb 3d peaks confirm qualitative incorporation of Nb, peak overlap of Cr and Te signals, together with the surface-sensitive nature of XPS, prevents precise quantification of the Nb concentration. Figure 1f shows EDS spectrum taken from the area (solid square) in the SEM image (Figure 1e) with Cr, Nb, Te peaks in the L and K series of $\text{Cr}_{0.8}\text{Nb}_{0.2}\text{Te}_2$ crystal. There are other peaks of O and K coming from air/oxidation and K residue during sample preparation, respectively. The EDS maps of Cr ($\text{K}\alpha_1$), Nb ($\text{L}\alpha_1$), and Te ($\text{L}\alpha_1$) in Figures 1g-i show their homogeneous distributions over the entire region of the crystal.

We performed additional EDS mapping using scanning transmission electron microscopy (STEM) and high-angle annular dark field (HAADF) on selected thin $\text{Cr}_{0.8}\text{Nb}_{0.2}\text{Te}_2$ flakes confirming the mixing of Nb into CrTe_2 crystal, see Figure S1.5 in the Supporting Information. Although, due to inherent limitations in SEM or STEM EDS, particularly in accurately measuring the content of lower doped crystals,^[44] it cannot be used here to quantify the exact Nb content. Electron energy loss spectroscopy (EELS) on selected $\text{Cr}_{0.8}\text{Nb}_{0.2}\text{Te}_2$ flakes confirm the distribution of Nb within the crystal similar to Cr and Te (see Figure S1.6 in the Supporting Information). Still, the resolution of our EELS-STEM, hindered by the thick (≥ 100 nm) nature of our flakes, is not enough to show the position of the Nb atoms near the Cr atoms. Future approaches such as exfoliating thinner (< 20 nm) flakes^[33,57] or epitaxially growing thin $\text{Cr}_{1-x}\text{Nb}_x\text{Te}_2$ crystals films^[34,58] may reveal the exact Nb concentration and position within the $\text{Cr}_{1-x}\text{Nb}_x\text{Te}_2$ crystals.

2.2. Static magnetic properties of $1T\text{-Cr}_{1-x}\text{Nb}_x\text{Te}_2$ ($x = 0 - 0.2$) crystals

To study the effect of Nb doping on the magnetic properties of $1T\text{-CrTe}_2$ crystals/flakes, we performed superconducting quantum interference device (SQUID, MPMS) and vibrating-sample magnetometer (VSM, PPMS Dynacool) magnetometry measurements. Zero field cooling (ZFC) and field cooling (FC) protocols were incorporated to assess the magnetic behavior of the crystals. Figure 2a displays the ZFC M - T curves of $\text{Cr}_{1-x}\text{Nb}_x\text{Te}_2$ ($x = 0, 0.05, 0.15, \text{ and } 0.2$) recorded at a magnetic field H of 30 mT and show a ferromagnetic-paramagnetic phase transition in a temperature range of 300 – 320 K. To confirm the nature of magnetism in $1T\text{-Cr}_{1-x}\text{Nb}_x\text{Te}_2$ crystals, the magnetization M is plotted vs H for $x = 0, 0.05, 0.15, \text{ and } 0.2$ Nb-doped crystals (Figure 2b). The hysteresis loops for all crystals show a saturation behavior at $H \sim 300$ mT and coercive magnetic field $H_c \sim 0.5 - 1.12$ mT (inset of Figure 2b), confirming the ferromagnetic nature of the

pristine^[32,35] and Nb-doped crystals.

The Curie temperature T_C , retrieved from derivatives of M - T curves in Figure 2a, is plotted as a function of Nb-doping factor x in Figure 2c. T_C decreases from 314.88 ± 0.28 K for pristine crystals to 300.26 ± 0.61 K for the $\text{Cr}_{0.8}\text{Nb}_{0.2}\text{Te}_2$ crystals. A similar trend for the saturation magnetization M_S vs Nb doping is observed, i.e., M_S decreases from 76.69 ± 1.17 kA/m for pristine crystals to 30.24 ± 0.28 kA/m for $\text{Cr}_{0.8}\text{Nb}_{0.2}\text{Te}_2$ crystals. We observe a noticeable variation of T_C and M_S for crystals doped with Nb content of $x = 0.1$ with averaged values of T_C and M_S that align well with the trends of the other compositions, see Supporting Information Section S2 and Figure S2.1. Such variation, evident from M - T and M - H curves, may be explained by the oxidation effect or by the instability of the $\text{Cr}_{0.9}\text{Nb}_{0.1}\text{Te}_2$ crystals.

The systematic reduction in T_C and M_S with increasing Nb doping, despite the contraction of the lattice along the ab plane (see Figure 6a), can be understood in terms of magnetic-site dilution and changes in exchange interactions. With increasing Nb content, non-magnetic Nb ions replace Cr sites, weakening the overall ferromagnetic coupling. In addition, the contraction of the ab -plane enhances the Cr–Cr direct exchange, which favors antiferromagnetic interactions, while the Cr–Te–Cr super-exchange that supports ferromagnetism becomes relatively less dominant. Simultaneously, the lattice expansion along the c -axis reduces the magnetic anisotropy energy, further lowering the Curie temperature, further discussed in Section S.2.4.

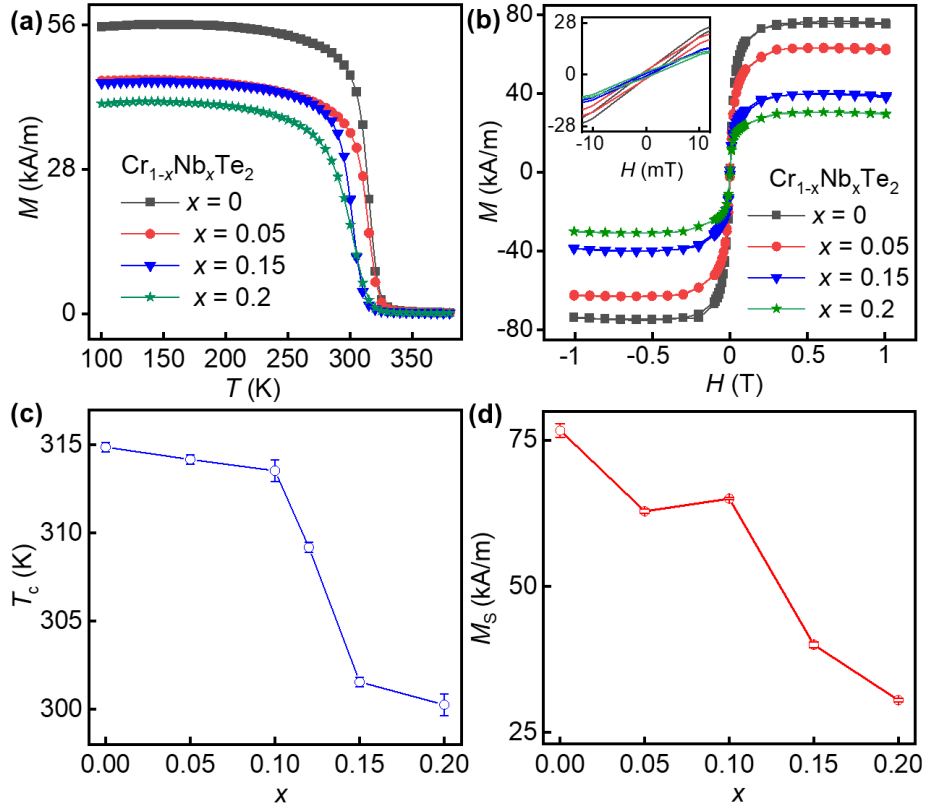


Figure 2: Magnetic measurements of $1T$ - $\text{Cr}_{1-x}\text{Nb}_x\text{Te}_2$ ($x = 0, 0.05, 0.15, 0.2$) crystals. (a) In-plane magnetization (M) versus temperature (T) curves at a magnetic field of 30 mT of $\text{Cr}_{1-x}\text{Nb}_x\text{Te}_2$ crystals, showing a ferromagnetic to paramagnetic phase transition in the range of 302 – 320 K. (b) In-plane M - H hysteresis loops measured at 300 K of $\text{Cr}_{1-x}\text{Nb}_x\text{Te}_2$ crystals. Inset of (b): zoomed M - H loops showing a coercive field in the range $\sim 0.5 - 1.12$ mT. Curie temperature T_C (c) and saturation magnetization M_S (d) as a function of Nb doping concentration factor x .

2.3. Spin dynamics of $1T\text{-Cr}_{1-x}\text{Nb}_x\text{Te}_2$ ($x = 0 - 0.2$) crystals and flakes

To study the spin dynamics of $1T\text{-Cr}_{1-x}\text{Nb}_x\text{Te}_2$ crystals and flakes, we performed FMR spectroscopy in a microwave (MW) frequency range of 1 – 40 GHz as a function of the applied magnetic field H (up to 0.6 T). Figures 3a and 3b show the schematic and picture of the coplanar waveguide (CPW) FMR setup, respectively, described in the Experimental Section. In Figures 3(c-g), we plot the normalized FMR (derivative MW absorption) signal versus the MW frequency and applied magnetic field for $\text{Cr}_{1-x}\text{Nb}_x\text{Te}_2$ ($x = 0, 0.05, 0.1, 0.15,$ and 0.2) crystals, done at room temperature (~ 297 K).

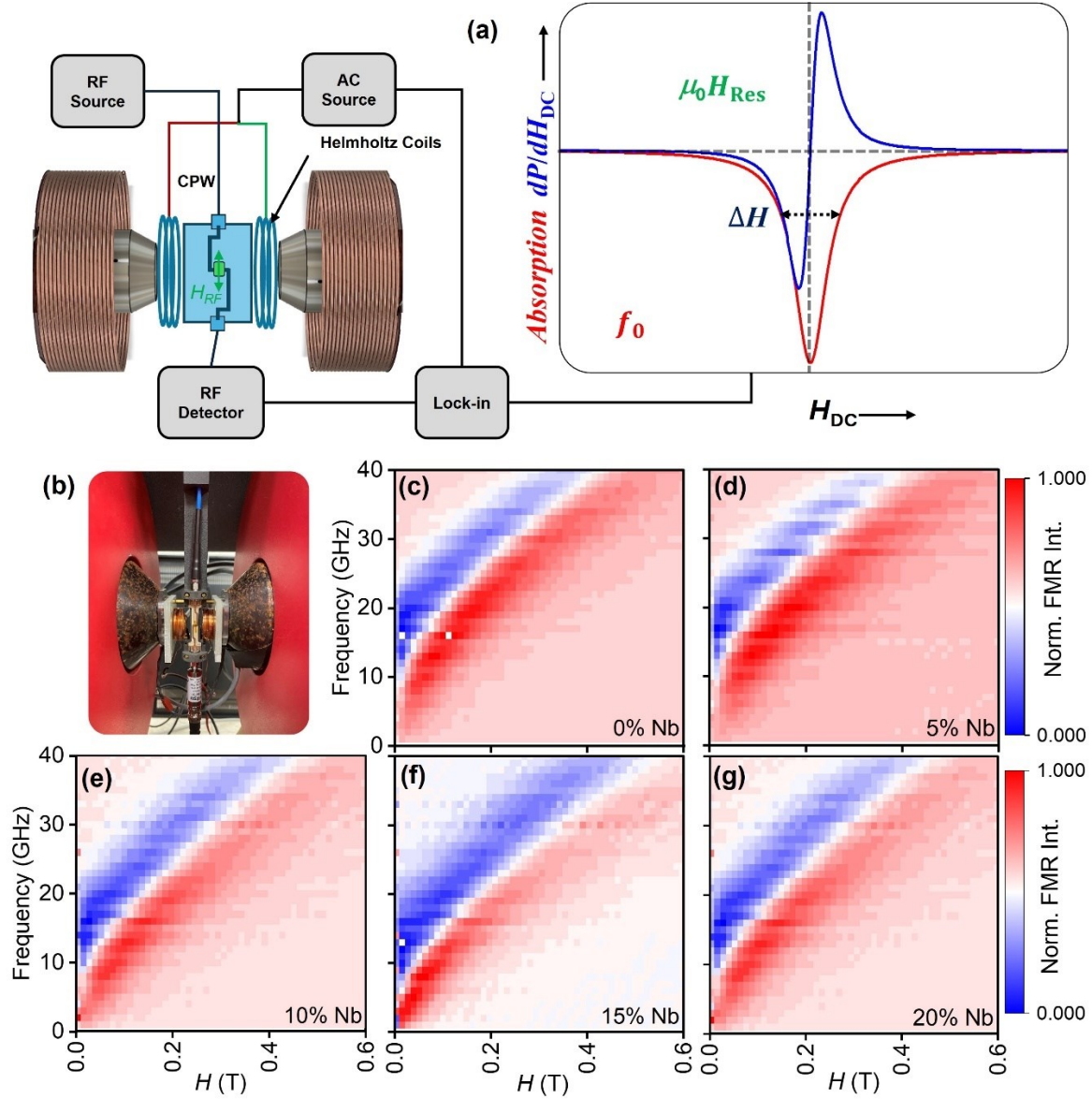


Figure 3. (a) Schematic representation of the FMR setup with diagram of MW absorption and lock-in detected derivative spectra. (b) A picture of the FMR setup: the sample is placed on top of a $50\ \Omega$ -matched CPW with one end connected to the MW source and the other to the MW detector. The CPW is placed between the poles of Helmholtz coils electromagnet. (c-g) color plots of the normalized FMR derivative absorption signal for $1T\text{-Cr}_{1-x}\text{Nb}_x\text{Te}_2$, $x = 0, 0.05, 0.1, 0.15,$ and 0.2 , respectively. The FMR spectra were measured over a frequency range of 1–40 GHz and a magnetic field range of 0 – 0.6 T.

The spin dynamics of the $1T\text{-Cr}_{1-x}\text{Nb}_x\text{Te}_2$ crystals can be described by the Landau-Lifshitz-Gilbert (LLG) equation:^[59]

$$\frac{\partial \mathbf{M}}{\partial t} = -\gamma \mathbf{M} \times \mathbf{H}_{\text{eff}} + \alpha \frac{\mathbf{M}}{M_S} \times \frac{\partial \mathbf{M}}{\partial t},$$

where \mathbf{M} is the magnetization vector, \mathbf{H}_{eff} is the effective magnetic field including the external magnetic field H , and anisotropy and exchange fields, and α is the Gilbert damping constant. γ is the gyromagnetic ratio, defined as $\gamma = -g\mu_B/\hbar$, where g is the Landé factor, μ_B is the Bohr magneton.

To deduce the effect of Nb doping on the magnetic anisotropy, damping, and Landé g -factor, the frequency dependence of the resonance field H_R is plotted in Figure 4a and fitted (solid line) with the Kittel formula for an in-plane sample as:^[59,60]

$$f = \left(\frac{\mu_0\gamma}{2\pi}\right) \sqrt{H_R(H_R + M_{\text{eff}})},$$

where μ_0 is the vacuum magnetic permeability and $M_{\text{eff}} = M_S - H_k$,^[60] H_k is the effective magnetic anisotropy field containing both anisotropy and exchange fields. For bulk crystals $H_k = 2K_{\text{eff}}/\mu_0 M_S$, where K_{eff} is the effective magnetic anisotropy. K_{eff} is $\sim 1.47 \pm 0.02 \times 10^5 \text{ J/m}^3$ for pristine $1T\text{-CrTe}_2$ crystals which is more than the measured value at 300 K of $0.49 \times 10^5 \text{ J/m}^3$ in ultrathin (thickness of 7ML) epitaxial $1T\text{-CrTe}_2$ films.^[34]

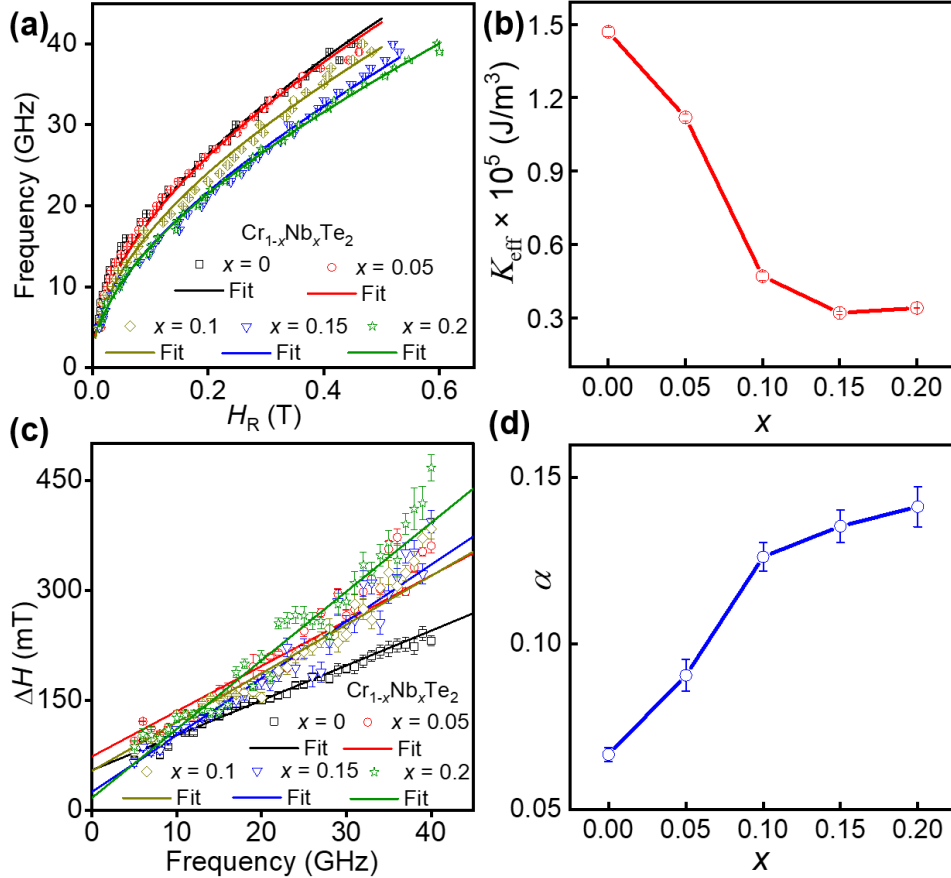


Figure 4. (a) Frequency dependence of the resonance field vs applied magnetic field for $\text{Cr}_{1-x}\text{Nb}_x\text{Te}_2$, $x = 0, 0.05, 0.1, 0.15,$ and 0.2 , respectively. The solid lines in (a) are fits using the Kittel formula for in-plane applied magnetic field. (b) K_{eff} versus Nb doping factor x . (c) Measured (scattered) FMR linewidth extracted from the plots in Figures 3(c-g), fitted (solid lines) with linear fits. (d) α vs Nb doping factor x .

The Nb doping strongly affects K_{eff} as shown in Figure 4b. K_{eff} decreases from $1.47 \pm 0.02 \times 10^5 \text{ J/m}^3$ for the parent pristine CrTe₂ crystals to $\sim 0.34 \pm 0.02 \times 10^5 \text{ J/m}^3$ for the Cr_{0.8}Nb_{0.2}Te₂ crystals, which is explained by the decrease in magnetic exchange coupling between Cr atoms upon Nb (bigger atoms) doping. Similar behavior is observed in the DFT calculations, discussed in Section 2.4. The Landé g -factor increases with increasing the Nb doping concentration as: $g = 2.00924$ for the pristine CrTe₂ and 2.125 for the Cr_{0.8}Nb_{0.2}Te₂ crystals. Similar effects were observed in the V-doped Fe_{1-x}V_x alloys.^[60]

To extract α , the FMR linewidth ΔH is plotted vs the MW frequency f in Figure 4c, and linear fitted (solid lines) as:^[61]

$$\Delta H = 4\pi\alpha f / \gamma\mu_0 + \Delta H_0,$$

where ΔH_0 is a constant. As shown in Figure 4d, α increases from 0.0666 ± 0.0021 for pristine CrTe₂ to 0.1413 ± 0.0060 for Cr_{0.8}Nb_{0.2}Te₂ crystals, respectively. Nb increases the damping due to the large size (0.68 Å) of the Nb atoms in comparison to the Cr (0.55 Å) atoms that creates disorder, which enhances spin-orbit coupling with Te layer and scattering of conduction electrons.^[31,32] The damping of the pristine and Nb doped CrTe₂ is comparable to ferromagnetic metallic (e.g., Co and CoPt₃)^[62,63] and ferrimagnetic insulating (e.g., TmIG)^[44,51] films.

We performed FMR spectroscopy of pristine CrTe₂ flakes (thickness ~ 100 nm). The CrTe₂ flakes (Figure 5a) were exfoliated from the pristine 1T-CrTe₂ crystals using vinyl blue tape.^[64,65] Figure 5b shows the derivative of the measured normalized FMR absorption spectrum versus the applied magnetic field H at a MW frequency of 18.5 GHz. The FMR curves at each MW frequency were fitted (solid lines in Figure 5b) to extract the resonance field H_R . The frequency dependence of H_R is plotted in Figure 5c and fitted with in-plane Kittel formula,^[59] giving an effective magnetization M_{eff} of 1.37 T. Due to the low volume of the magnetic flake, it is not possible to use standard bulk magnetometry techniques (e.g., SQUID) to deduce M_S of the CrTe₂ flakes. In reference [33], NV magnetometry was used to deduce $M_S \sim 27$ kA/m for thin (thickness of ~ 20 nm) CrTe₂ flake from magnetic stray-field measurements.^[33] This value is way less than the measured value of ~ 76.7 kA/m of the pristine CrTe₂ crystals. By assuming a variation of M_S of the 100-nm flake in the range of $27 - 76$ kA/m, and by using $M_{\text{eff}} = M_S - H_K$, we deduce an effective magnetic anisotropy K_{eff} in the range of $0.25 \times 10^5 - 0.5 \times 10^5 \text{ J/m}^3$, which is close to the value of $\sim 0.49 \times 10^5 \text{ J/m}^3$ obtained at 300 K in 7 ML CrTe₂ films.^[34] The CrTe₂ flake's magnetic anisotropy is less than the bulk (crystal) value of $\sim 1.47 \times 10^5 \text{ J/m}^3$, explained by magnetic anisotropy thickness dependence effects as:^[34,35,66]

$$K_{\text{eff}} = K_v + K_s/t - K_d,$$

where K_v is the volume anisotropy, K_s is the surface/interface anisotropy, $K_d = 1/2 \mu_0 M_S^2$ is the demagnetization/shape anisotropy, and t is the thickness of the film/flake. K_s and K_d dominates in thin films/flakes,^[59,60] whereas K_v dominates in bulk CrTe₂ crystals.

To extract the damping constant α of the CrTe₂ flakes, the FMR linewidth ΔH is plotted versus the frequency f in Figure 5d and linear fitted. α is ~ 0.13 , higher than the bulk value of ~ 0.0665 , that is explained by surface (roughness, interface) effects.^[67]

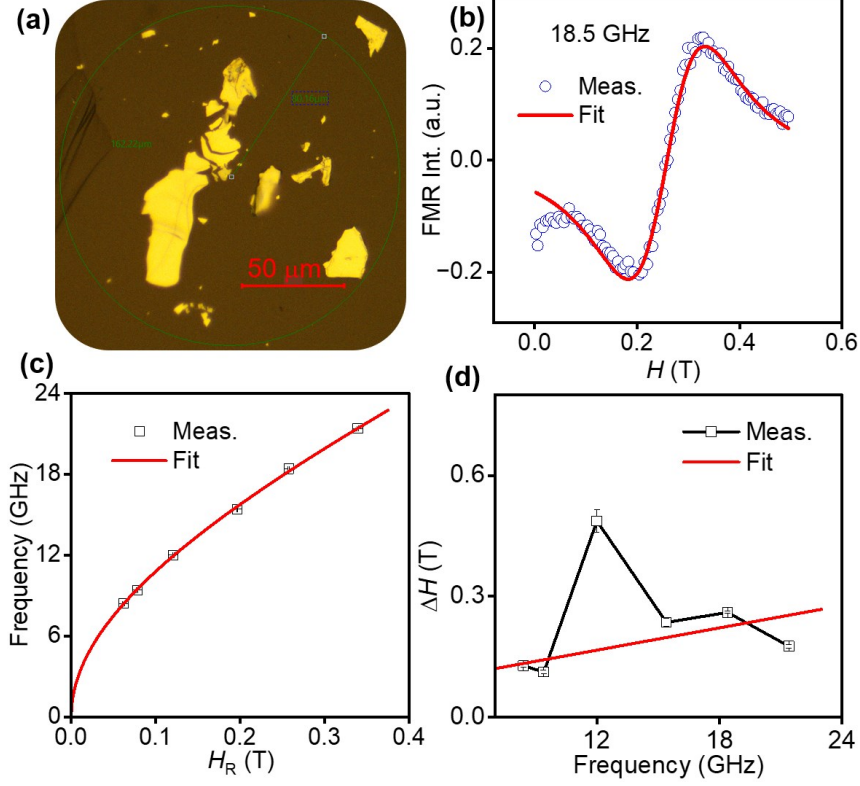


Figure 5. (a) Optical image of $1T\text{-CrTe}_2$ flakes, exfoliated from bulk $1T\text{-CrTe}_2$ crystal and transferred to the CPW antenna for FMR measurements. (b) FMR intensity vs applied magnetic field at a MW frequency of 18.5 GHz of CrTe_2 flakes in (a). (c) Measured (scattered) and fitted (solid line) frequency dependence of the resonance field H_R vs applied magnetic field. (d) Measured (scattered) FMR linewidth ΔH extracted from the plot in (c), fitted (solid lines) with linear fit to extract α .

2.4. Density Functional Theory Calculations

To study the effect of Nb doping on the magnetic properties of $1T\text{-Cr}_{1-x}\text{Nb}_x\text{Te}_2$ crystals, electronic structure calculations were performed at 0 K temperature within the framework of DFT using the plane-wave pseudopotential method, as implemented in *Quantum ESPRESSO*.^[68] Fully relativistic optimized norm-conserving pseudopotentials^[69] were employed, and the exchange–correlation functional was treated within the generalized gradient approximation (GGA).^[70] Magnetic effects were accounted for through the inclusion of spin–orbit coupling in the pseudopotentials. The virtual crystal approximation (VCA)^[71] was applied to model the Nb doping. A kinetic energy cutoff of 100 Ry was used for the plane-wave basis set, and Gaussian smearing with a broadening of 0.01 Ry was adopted. Brillouin-zone integrations were performed over a $24 \times 24 \times 15$ Monkhorst–Pack k -point mesh in the irreducible Brillouin zone to ensure convergence for all bulk calculations. For each Nb doping concentration factor x , the primitive unit cell structure was fully relaxed, and the corresponding lattice constants are shown in Figure 6c. The Hamiltonian of the system is expressed as:

$$H = - \sum_{i \neq j} J_{\parallel} \mathbf{s}_i \cdot \mathbf{s}_j - \sum_{i \neq j} J_{\perp} \mathbf{s}_i \cdot \mathbf{s}_j - K \sum_i (\hat{\mathbf{z}} \cdot \mathbf{s}_i)^2,$$

where \mathbf{s} denotes the normalized spin vector, J_{\parallel} is the exchange coupling between in-plane nearest neighbors (Figure 6a), J_{\perp} is the exchange coupling between adjacent layers (Figure 6b), and K is

the magnetic anisotropy energy per magnetic atom. The exchange interaction J_{\parallel} and J_{\perp} were calculated using supercells of size $2 \times 2 \times 1$ (Figure 6a) and $1 \times 1 \times 2$ (Figure 6b), respectively, by evaluating energy difference between ferromagnetic (FM) and AFM magnetic configurations, with the results shown in Figure 6d. The effective magnetic anisotropy K_{eff} (Figure 6f) is obtained from the total energy difference between in-plane and out-of-plane FM configurations, see Supporting Information Section S3. The calculated values of K_{eff} are approximately one order of magnitude higher than the measured values. This can be related to many factors such as temperature effect^[34] (0 K for theory and 297 K for the measurements) and by the crystal imperfections (different sizes/shapes). However, the general trend of the Nb effect on the magnetic moment (Figure 6e) and magnetic anisotropy still agrees well with the measurements.

The observed trend also correlates with theoretical calculations of the exchange parameters (Figure 6d), showing a monotonic decrease in J_{\parallel} (in-plane exchange) and an increase in J_{\perp} (interlayer exchange). This can be understood by the fact that a relatively small lattice parameter a favors direct antiferromagnetic Cr–Cr exchange over the indirect ferromagnetic Cr–Te–Cr exchange.^[32] Conversely, the increase of J_{\perp} arises from reduction of magnetic anisotropy by substituting Cr^{4+} (0.55 Å) with the larger Nb ion (0.68 Å), which enhances spin–orbit coupling with the Te layer and support the ferromagnetic character of the systems. These findings highlight the tunability of CrTe_2 's magnetic properties, with Nb doping enabling modification of magnetic interactions while maintaining robust ferromagnetic order at room temperature.

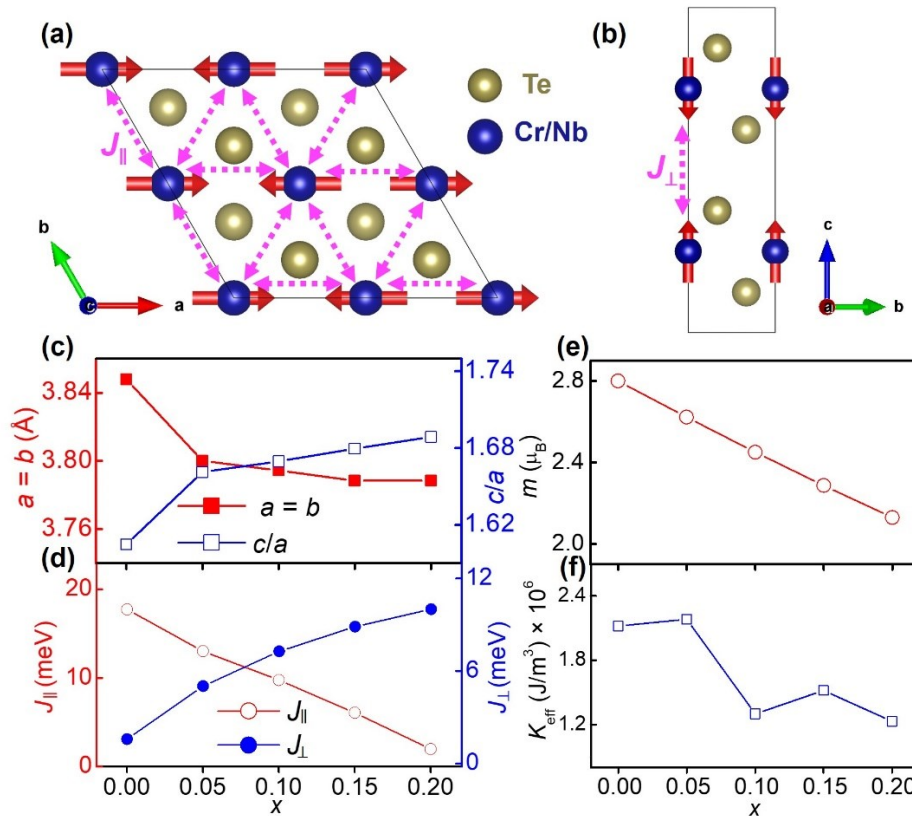


Figure 6. Top view (a) and side view (b) of $\text{Cr}_{1-x}\text{Nb}_x\text{Te}_2$ exchange interactions J_{\parallel} and J_{\perp} between neighboring magnetic atoms, indicated by the magenta arrows. (c-f) Evolution of parameters as a function of Nb concentration: (c) lattice constant $a = b$ and c/a , (d) exchange interactions J_{\parallel} and J_{\perp} , (e) magnetic moment m , and (f) effective magnetic anisotropy K_{eff} .

3. Conclusions

In conclusion, we have demonstrated that the spin dynamics of $1T$ -CrTe₂ crystals can be systematically engineered by Nb substitution in Cr_{1-x}Nb_xTe₂ ($x = 0 - 0.2$), while preserving robust room-temperature ferromagnetism. Nb doping provides an effective route to modify magnetic interactions, leading to controlled changes in both static and dynamic magnetic properties. With increasing Nb content, the Curie temperature, saturation magnetization, and magnetic anisotropy are reduced, while robust ferromagnetism persists above room temperature ($T_C \sim 300$ K for the Cr_{0.8}Nb_{0.2}Te₂). Structural characterization using XRD and HRTEM reveals a Nb-induced lattice expansion along the c axis without degradation of crystallinity quality. DFT calculations reproduce these trends and attributed them to a reduction of both intralayer and interlayer exchange interactions between Cr atoms arising from a larger atomic radius of Nb compared to Cr.

Most importantly, Nb doping strongly tailors the dynamic magnetic response. FMR measurements reveal wide-band tunability of the resonance frequencies over 5 – 40 GHz, accompanied by only a modest increase of the Gilbert damping constant α to 0.066 – 0.14, remaining comparable to values reported for ferromagnetic metals^[62,63] and ferrimagnetic insulators.^[44,51] These characteristics establish Nb-doped $1T$ -CrTe₂ as a promising vdW ferromagnet for magnonic applications, extending its functionality beyond conventional spintronics^[34] to magnon spintronics^[43] and topological magnonics.^[45,46]

FMR measurements on $1T$ -CrTe₂ flakes revealed reduced resonant frequencies down to ~ 2 GHz at low applied magnetic field (~ 3 mT), indicating additional tunability of the dynamic magnetic properties through thickness control. Although achieving homogeneous exfoliation of CrTe₂ flakes^[33] remains challenging, controlled exfoliation assisted by thin Al₂O₃ capping layers^[72,73] may enable the fabrication of large-area ultrathin Cr_{1-x}Nb_xTe₂ flakes. Such flakes provide a pathway to exploit Cr_{1-x}Nb_xTe₂ as a 2D vdW magnetic platform for magnonics.^[37,74] Finally, integration with diamond^[16-18] and/or hBN^[19,20] substrates hosting spin qubits could enable proximity-driven spatial mapping of their spin-wave modes, opening avenues toward quantum magnonics and hybrid quantum architectures.^[47-51]

4. Experimental Section

Samples preparation: A stoichiometric mixture of high-purity potassium, chromium, niobium, and tellurium was prepared according to the desired doping level (x) under an argon atmosphere in a glove box. The mixture was loaded into evacuated quartz tubes to avoid oxidation and sealed under vacuum. The sealed tubes were heated to 900 °C in 24 hours and maintained at this temperature for eight days to ensure complete reaction. After the heat treatment, the tubes were allowed to cool slowly to room temperature at a rate of 80 °C/hour. After opening the tubes in the glove box, the potassium (K) atoms were removed via a deintercalation process.^[32] The resulting products consisted of dark, metallic-luster platelets and fine powders, which were handled in the glove box to prevent oxidation, Figure S1 (Supporting Information).

Ferromagnetic Resonance spectroscopy: Broadband Ferromagnetic Resonance (FMR) spectroscopy was performed on $1T$ -Cr_{1-x}Nb_xTe₂ ($x = 0 - 0.2$) crystals and flakes by measuring the change in microwave (MW) power absorption at various MW frequencies (1 – 40 GHz) as a function of applied magnetic field (see Figure 3). The samples were mounted on a copper Coplanar Waveguide (CPW) with a center conductor width of 0.4 mm and a gap of 0.2 mm, oriented in such that the microwave RF magnetic field is perpendicular to the static magnetic field. The signal generator generates MW frequencies ranging from 1 to 40 GHz. Electromagnets apply the static

magnetic field and are continuously monitored using a Hall probe. As the magnetic field was swept through the resonance, the magnetization vector precessed at resonance, it absorbed the MW energy, resulting in a decrease in the transmitted power. The power change was detected and converted into a DC voltage by a high-frequency MW detector. To improve the signal-to-noise ratio, a Lock-in Amplifier-based detection was employed. The applied magnetic field was modulated at 77 Hz with a 5 mT amplitude using a pair of Helmholtz coils. The recorded spectra represent the derivative of the RF absorption power. All the recorded data were background-subtracted, numerically integrated, and fitted with a Lorentzian function to extract the resonance magnetic field and the FMR linewidth.

Acknowledgements

K.A., J.W., and A.L. acknowledge the National Science Foundation (NSF) through Award 2328822. A.L. thanks for the additional support from NSF Award 2521415. A.L. and E.Y.T. acknowledge the University of Nebraska-Lincoln (UNL) Grand Challenges catalyst award entitled “Quantum Approaches addressing Global Threats”. Theoretical modeling at UNL was supported by NSF through the EPSCoR RII Track-1 program under Award OIA-2044049 (M.A.E., K.H., E.Y.T.) and the U.S. Department of Energy, Office of Science, Office of Basic Energy Sciences, through the DOE EPSCoR program under Award No. DE-SCSC0026103 (K.H., E.Y.T.). The research done at UNL was performed in part in the Nebraska Nanoscale Facility: National Nanotechnology Coordinated Infrastructure and the Nebraska Center for Materials and Nanoscience (and/or NERCF), supported by NSF Award 2025298. Computations were performed at the University of Nebraska Holland Computing Center. Part of the work was performed, in part, at the Center for Integrated Nanotechnologies, an Office of Science User Facility operated for the U.S. Department of Energy (DOE) Office of Science. Los Alamos National Laboratory, an affirmative action equal opportunity employer, is managed by Triad National Security, LLC for the U.S. Department of Energy’s NNSA, under contract 89233218CNA000001.

Conflict of Interest

The authors declare no conflict of interest.

Author Contributions

A.L., K.A. and J.W. conceived the concept, designed the experiments, and supervised the project. D.R.L performed the magnetic (SQUID, VSM) measurements, with assistance from J.K., R.T., and A.L. K.P., Z.H., and J.W. synthesized the CrNbTe₂ crystals and performed XRD measurements. J.K. analyzed the XRD data and fitted the curves. P.B.K., A.E.A., and K.A. performed FMR measurements. M.A.E., K.H., and E.Y.T. conducted DFT calculations. B.T. performed SEM, EDS, and HRTEM. S.L. and S.-H.L performed XPS. J.W. performed EELS on selected Cr_{1-x}Nb_xTe₂ crystals/flakes. A.L. wrote the manuscript with contributions and feedback from all authors.

Data Availability Statement

The data that support the findings of this study are available from the corresponding author upon reasonable request.

Keywords

CrTe₂, magnetometry, magnetism, ferromagnetic resonance spectroscopy.

Supporting Information

Section 1. Synthesis and characterization of 1T-Cr_{1-x}Nb_xTe₂ crystals

S1.1 Growth of Cr_{1-x}Nb_xTe₂ ($x = 0.05 - 0.2$) crystals

1T-CrTe₂ and 1T-Cr_{1-x}Nb_xTe₂ ($x = 0.05 - 0.2$) crystals were synthesized by direct solid-state reaction^[52] of the constituent elements of K, Cr, Nb, and Te, detailed in Figure S1.1 and the main text.

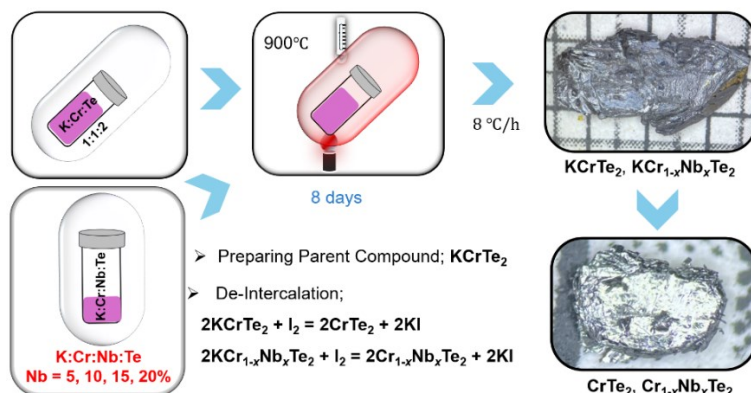


Figure S1.1. Synthesis of CrTe₂ and Cr_{1-x}Nb_xTe₂ ($x = 0.05 - 0.2$) crystals using solid-state reaction method.

S1.2 X ray diffraction of Cr_{1-x}Nb_xTe₂ ($x = 0.05 - 0.2$) crystals

X ray diffraction (XRD) measurements were collected at room temperature using a Rigaku Mini Flex 6G diffractometer with Cu-K α radiation ($\lambda = 1.5406 \text{ \AA}$) in the range of $2\theta = 10^\circ - 60^\circ$, at a scan step of 0.05° with 10 seconds of exposure time. Figure S.1.2 depicts the structural information of the compounds 1T-Cr_{1-x}Nb_xTe₂ ($x = 0, 0.05, 0.10, 0.15, 0.20$). Lattice parameters (a , b , and c) of the samples (see Table S1) were obtained by analysis of the diffraction pattern ($2\theta = 10^\circ$ to 60°) by the Le Bail method using the FullProf Suite program.^[75] The XRD peaks of all the compositions in Figure S1.2a are well fitted with the space group $P\bar{3}m1$, No. 164, indicating the single-phase formation of the synthesized crystals. In Figure S1.2b, a shift of the Bragg peak towards lower angles with increasing the Nb concentration is observed, indicating lattice expansion due to the incorporation of larger Nb atoms to replace Cr atoms in the lattice. As shown in Figure S1.2c, the lattice parameter ($a = b$) decreases from 3.7803 \AA to 3.7761 \AA with Nb doping up to 20%. A successive increase in the c/a ratio (Figure S1.2c) with higher Nb concentration further confirms the lattice expansion along the crystallographic c -axis. The deduced density of the Cr_{1-x}Nb_xTe₂ ($x = 0 - 0.2$) crystals, plotted in Figure S1.2d, increases with the increase in the Nb concentration, explained by substituting the lighter Cr atoms with the heavier Nb atoms.

Table S1: Lattice parameters obtained from X-ray profile fitting

Crystal composition	Lattice parameters ($a=b$) (\AA), $\alpha=\beta=90^\circ$ and $\gamma=120^\circ$	Lattice parameter c (\AA)	c/a ratio
CrTe ₂	3.7803(1)	6.0936(2)	1.6119(0)
Cr _{0.95} Nb _{0.05} Te ₂	3.7808(2)	6.0893(3)	1.6105(1)
Cr _{0.90} Nb _{0.10} Te ₂	3.7778(1)	6.1031(3)	1.6155(1)
Cr _{0.85} Nb _{0.15} Te ₂	3.7785(1)	6.1210(3)	1.6199(1)
Cr _{0.80} Nb _{0.20} Te ₂	3.7761(2)	6.1428(5)	1.6267(1)

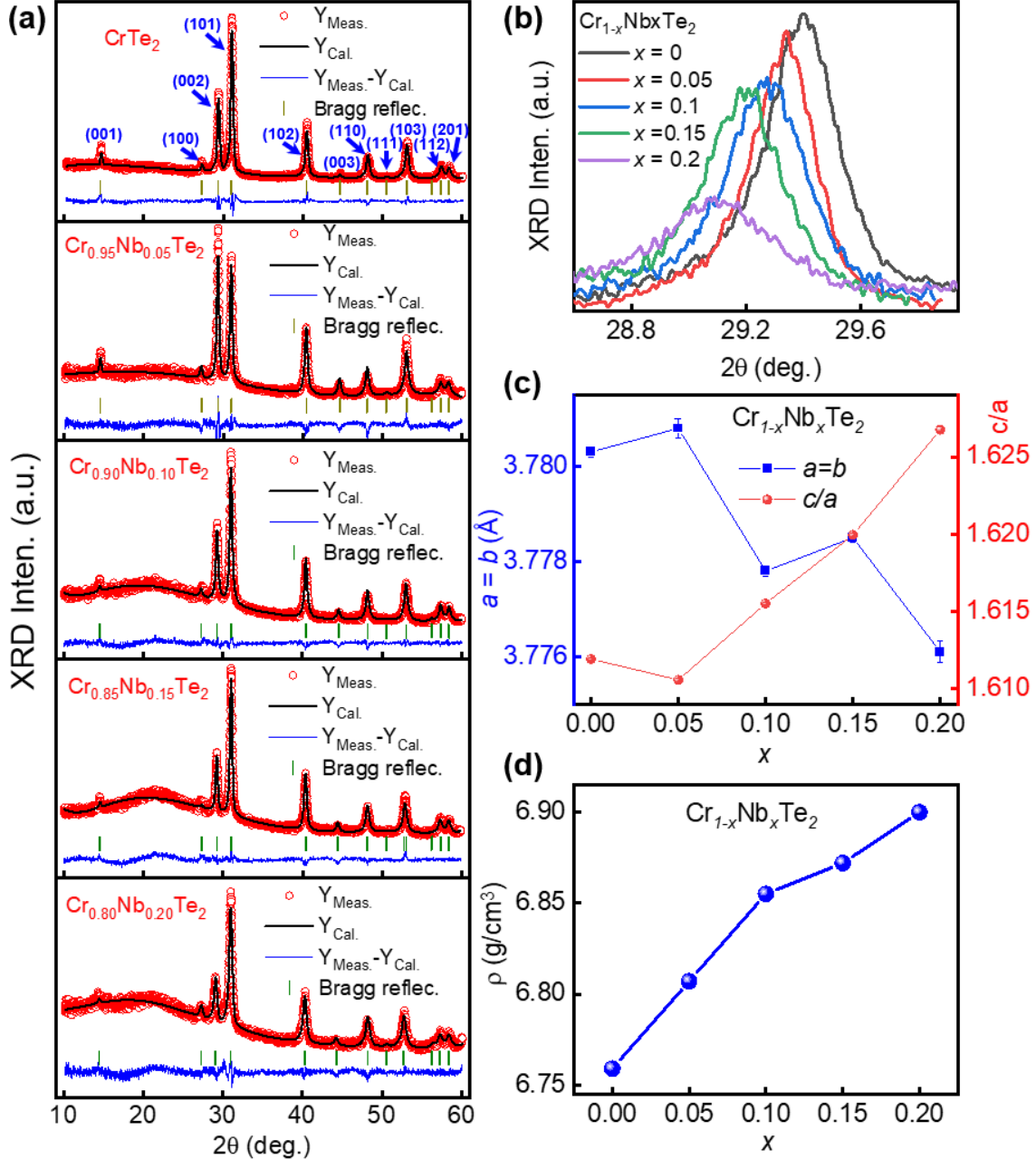


Figure S1.2. (a) Measured (scattered) and fitted (solid line) XRD spectroscopy data for $1T\text{-Cr}_{1-x}\text{Nb}_x\text{Te}_2$ ($x = 0, 0.05, 0.1, 0.15, \text{ and } 0.2$) crystals. The fitting was refined by using the Le-Bail method with $P\bar{3}m1$ symmetry and the fitted parameters are listed in Table S1. (b) The XRD peak at $2\theta \sim 29^\circ$, corresponding to (002) plane, shifts towards lower diffraction angles with increasing Nb doping concentration. (c) The variation of the lattice parameters a and b , and the ratio c/a , as a function of the Nb concentration. (d) Deduced density of the $\text{Cr}_{1-x}\text{Nb}_x\text{Te}_2$ crystals as a function of the Nb concentration in the range $x = 0 - 0.2$.

Table S.2 contains the values of Miller indices (h , k , and l) of the different planes, XRD angle 2θ , and interplane spacing (d_{hkl}) values of $\text{Cr}_{0.8}\text{Nb}_{0.2}\text{Te}_2$ crystal. The rectangles in Table S2 show the information of the planes mentioned in the main text.

Table S2: Deducing the (*hkl*) planes from the XRD peaks fitting

No.	Code	<i>h</i>	<i>k</i>	<i>l</i>	luIt	Hw	ETA/M	2theta/TOF	Icalc	Iobs	Sigma	StrFactor^2	d-hk1	CORR
1	1	0	0	1	2	0.432319	0.445104	14.407	0.0	0.0	0.000	0.0000	6.142813	1.000000
2	1	1	0	0	6	0.470760	0.686085	27.247	39.5	39.9	2.573	424.1077	3.270239	1.000000
3	1	0	0	2	2	0.477940	0.719894	29.049	159.9	160.5	1.940	5912.7222	3.071407	1.000000
4	1	0	1	1	6	0.485993	0.755632	30.953	226.6	227.4	1.642	3201.5139	2.886661	1.000000
5	1	1	0	1	6	0.485993	0.755632	30.953	226.6	227.4	1.642	3201.5139	2.886661	1.000000
6	1	0	1	2	6	0.532042	0.930097	40.249	106.0	106.3	1.324	2664.3362	2.238806	1.000000
7	1	1	0	2	6	0.532042	0.930097	40.249	106.0	106.3	1.324	2664.3362	2.238806	1.000000
8	1	0	0	3	2	0.554943	1.004167	44.195	38.4	38.5	1.107	3575.6582	2.047604	1.000000
9	1	1	1	0	6	0.579938	1.078482	48.155	163.5	164.0	1.762	6159.2036	1.888074	1.000000
10	1	1	1	1	12	0.595916	1.123062	50.530	14.6	14.5	0.460	305.9398	1.804748	1.000000
11	1	0	1	3	6	0.611158	1.163757	52.699	98.2	98.7	0.954	4540.4829	1.735481	1.000000
12	1	1	0	3	6	0.611158	1.163757	52.699	98.2	98.7	0.954	4540.4829	1.735481	1.000000
13	1	2	0	0	6	0.637195	1.229649	56.209	21.9	21.9	0.454	1183.1703	1.635120	1.000000
14	1	1	1	2	12	0.645054	1.248727	57.226	80.9	81.5	0.996	2301.7917	1.608466	1.000000
15	1	0	2	1	6	0.653925	1.269846	58.351	42.0	42.0	0.497	2577.6838	1.580099	1.000000
16	1	2	0	1	6	0.653925	1.269846	58.351	42.0	42.0	0.497	2577.6838	1.580099	1.000000

BRAGG R-Factors and weight fractions for Pattern # 1

S1.3 Transmission electron microscopy of 1T-Cr_{0.8}Nb_{0.2}Te₂ flakes

High resolution transmission electron microscopy (HRTEM) images (Figure S1.3) of 1T-Cr_{0.8}Nb_{0.2}Te₂ flakes show lattice fringes from multiple regions. Variations in lattice orientation, contrast, and fringe continuity indicate a polycrystalline structure composed of numerous nanoscale domains rather than a single uniform crystal.

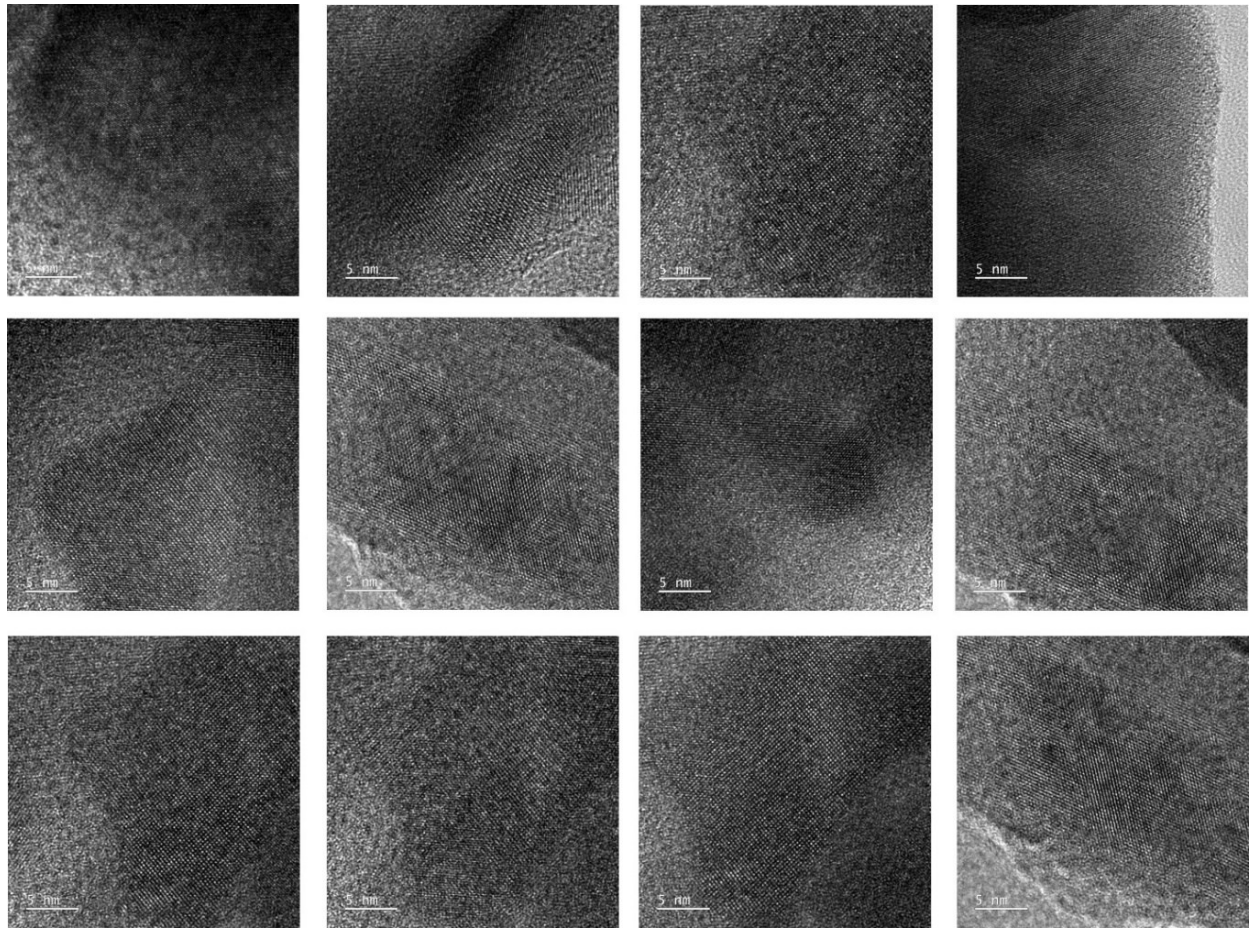


Figure S1.3.1. HRTEM images of 1T-Cr_{0.8}Nb_{0.2}Te₂ crystals.

Zoomed HRTEM image of one of the $\text{Cr}_{0.8}\text{Nb}_{0.2}\text{Te}_2$ nanoflakes in Figure S1.3.2 confirms the well-resolved (100) lattice fringes consistent with the expected interplanar spacing ($d \approx 0.32$ nm).

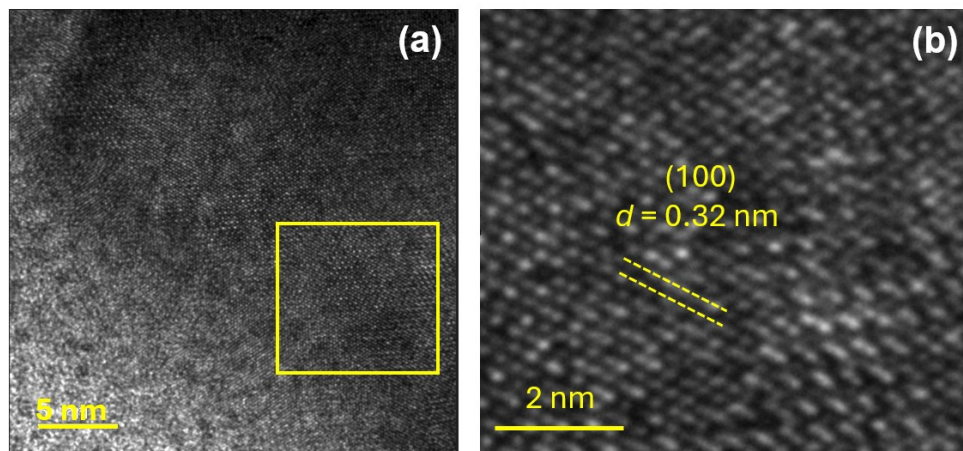


Figure S1.3.2. (a) HRTEM image of $1T\text{-Cr}_{0.8}\text{Nb}_{0.2}\text{Te}_2$ crystal showing different crystal orientations. (b) Zoomed HRTEM image of the region in (a) highlighted by a solid square showing the (100) lattice fringes.

S1.4 X-ray photoelectron spectroscopy of $\text{Cr}_{1-x}\text{Nb}_x\text{Te}_2$ crystals

X-ray photoelectron spectroscopy (XPS) measurements were performed using Thermo Scientific Al K-Alpha XPS system under high vacuum with pressure of $\sim 10^{-9}$ mbar.^[44,56] Spectral data were collected with Avantage software. To minimize surface charging during measurement, both dual electron and argon ion flood guns were applied maintaining the Ar pressure of 2×10^{-8} mbar. The X-ray beam had a spot size of 400 μm , and high-energy resolution spectra were obtained with a pass energy of 50 eV, a step size of 0.1 eV and a dwell time of 50 ms, respectively.^[44,56] Multiple scans were performed for each element to improve the signal to noise ratio, typically ranging from 20 to 100 sweeps. All spectra were referenced to C1s peak at 284.8 eV to correct for residual charging. Figure S1.4(a-b) shows XPS peaks of Te and Cr in pristine and $\text{Cr}_{0.8}\text{Nb}_{0.2}\text{Te}_2$ crystals, respectively. The binding energies of Te $3d_{5/2}$ and Te $3d_{3/2}$ doublets are ~ 572.5 eV and 582.8 eV, respectively. The binding energies of Cr $2p_{3/2}$ and Cr $2p_{1/2}$ doublets ~ 575.8 eV and 586.4 eV, respectively, consistent with Reference [35].

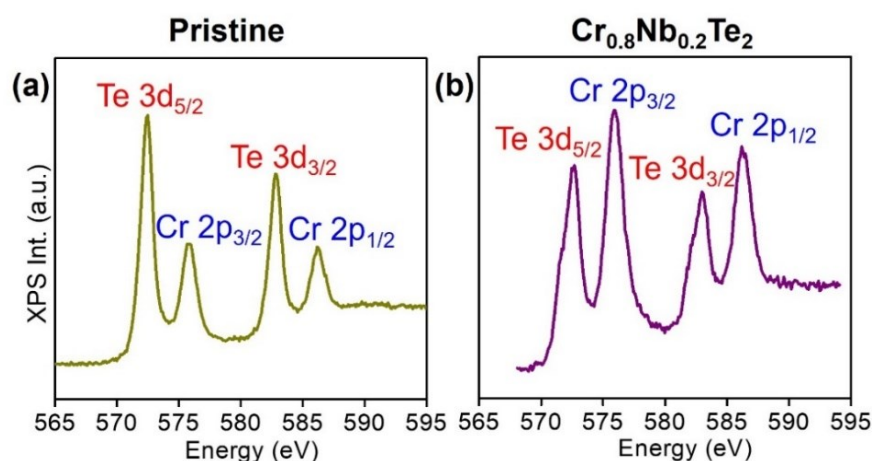


Figure S1.4. High resolution XPS spectra of $1T$ -CrTe₂ (a) and $1T$ -Cr_{0.8}Nb_{0.2}Te₂ (b).

S1.5 Energy-dispersive X-ray spectroscopy measurements

To further verify the Nb incorporation into the $1T$ -CrTe₂ lattice, we performed energy-dispersive X-ray (EDS) mapping using scanning transmission electron microscopy (STEM) coupled with high-angle annular dark-field (HAADF) imaging on selected thin Cr_{0.8}Nb_{0.2}Te₂ nanoflakes. The resulting elemental maps confirm the successful mixing of Nb within the CrTe₂ crystal structure, see Figure S1.5.

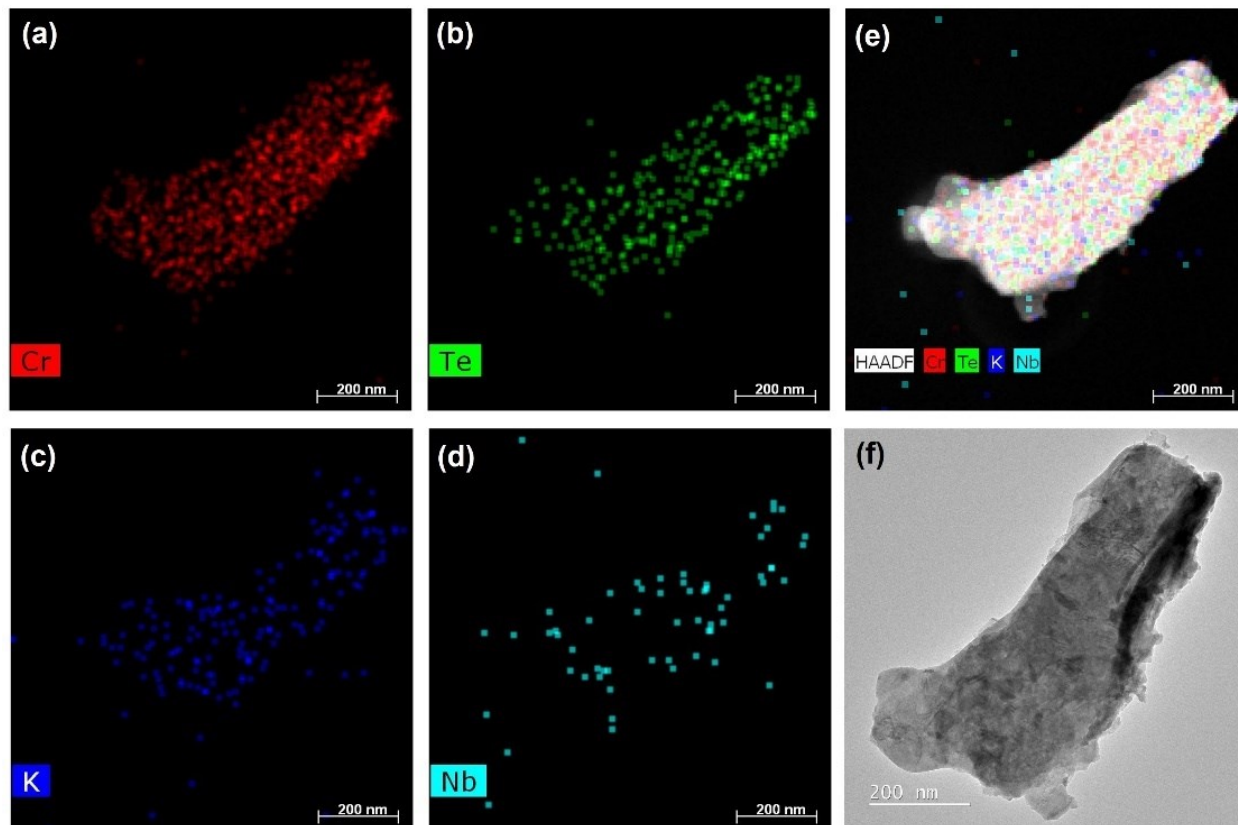


Figure S1.5. (a–d) EDS elemental maps of Cr, Te, K, and Nb in a Cr_{0.8}Nb_{0.2}Te₂ nanocrystal, each displayed in a separate color channel to highlight their spatial distribution. (e) Overlapped HAADF-STEM/EDS composite map showing the combined Cr, Te, K, and Nb signals, confirming uniform elemental dispersion within the crystal. (f) Corresponding HAADF-STEM image of the analyzed nanoflake.

S1.6 Electron energy loss spectroscopy

We performed scanning transmission electron microscopy (STEM) and electron energy loss spectroscopy (EELS) on a selected $1T$ -Cr_{0.8}Nb_{0.2}Te₂ nanoflake to check the distribution of Nb atoms. Scanning transmission electron microscopy (STEM) was performed using a Titan ETEM operating at 300 keV. Electron energy loss spectroscopy (EELS) was carried out using a Gatan Biocontinuum/K3-IS. Figure S1.6 confirms a homogeneous distribution of Cr, Te, and Nb within the crystal. Due to the overlap of Cr and Te, it is hard to extract the exact elemental concentrations, and additional deconvolution and principal component analysis are needed.^[76]

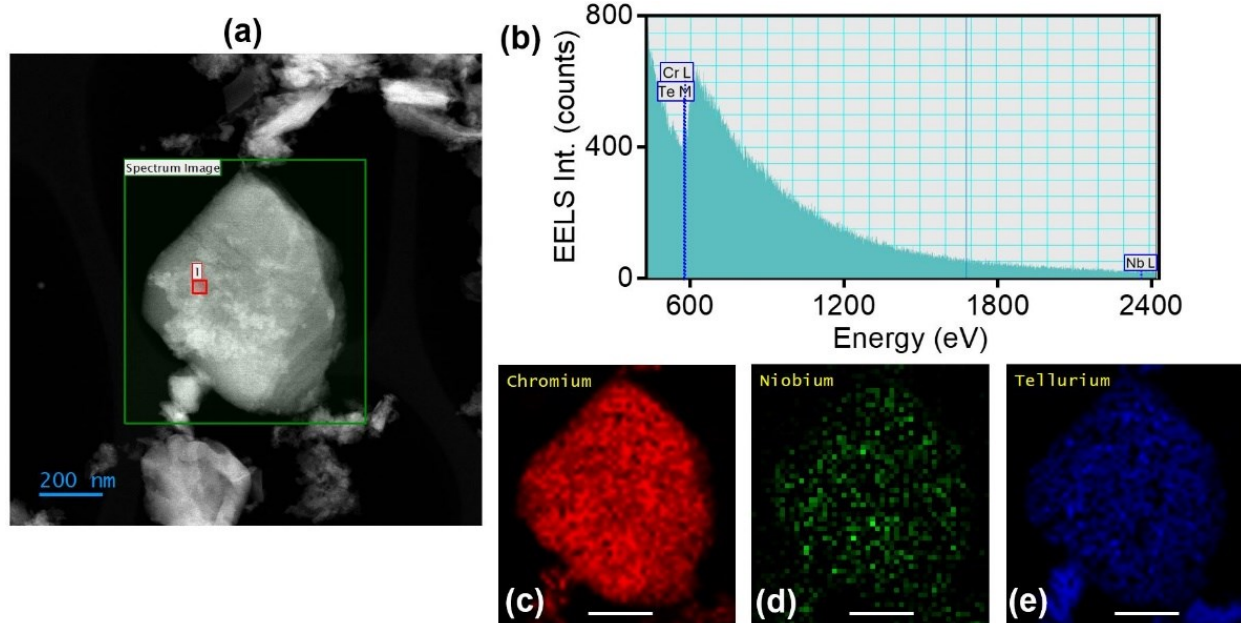


Figure S1.6. (a) STEM-HAADF image of $1T\text{-Cr}_{0.8}\text{Nb}_{0.2}\text{Te}_2$ nanoflake. (b) EELS spectrum showing the overlap of Cr and Te elements. (c-e) Element maps of Cr, Nb, and Te, respectively

Section S2: Additional magnetic measurements on $\text{Cr}_{0.9}\text{Nb}_{0.1}\text{Te}_2$

As discussed in the main text, the $1T\text{-Cr}_{0.9}\text{Nb}_{0.1}\text{Te}_2$ crystals exhibit ferromagnetic behavior with different Curie temperature (T_C) values in the range of 309 – 318 K (Figures S2.1a-b) and saturation magnetization (M_s) in the range of 43 – 76 kA/m (Figures S2.1c-d). This can be explained by the instability of this composition, size of the microcrystals, or oxidation effects. We note that the $\text{Cr}_{0.9}\text{Nb}_{0.1}\text{Te}_2$ powder was obtained by crashing the big freshly made $\text{Cr}_{0.9}\text{Nb}_{0.1}\text{Te}_2$ crystal labeled as “Big cry.”. While there are no structural changes observed from EELS and EDS (discussed above) in the powder, its magnetic properties are slightly affected, manifested by a decrease (from 76 kA/m to 43 kA/m) in the saturation magnetization and an increase (from ~1 mT to ~5 mT) in the coercive field (see inset of Figure S2.1c), that may be explained by size effects.^[77,78]

Figure S.2.2 depicts T_C , the magnetic anisotropy (H_A) extracted from FMR spectroscopy, and the c/a ratio deduced from XRD refinements for $\text{Cr}_{1-x}\text{Nb}_x\text{Te}_2$ ($x = 0.05 - 0.2$) crystals. T_C , H_A , and c/a change slightly until $x = 0.1$. Then, they change drastically for Nb concentration $x \geq 10\% - 20\%$, that is closely related to the effect of the increasing c/a ratio upon replacing the small (0.55 Å) Cr atoms with larger (0.68 Å) Nb atoms.^[32] Generally, in layered materials, in-plane bonds are much stiffer and stronger compared to the weak van der Waals forces that bind the layers together. The lattice strain from the larger Nb atoms is thus more easily accommodated by an expansion of the interlayer spacing (the c -axis parameter). The expansion of c/a ratio also alters the environment around the Cr and Te atoms, which leads to a change in the spin-orbit coupling.^[35] Since spin-orbit coupling strongly influences the magnetic anisotropy energy, it is a key parameter that also affects the Curie temperature (discussed below in Section S3).

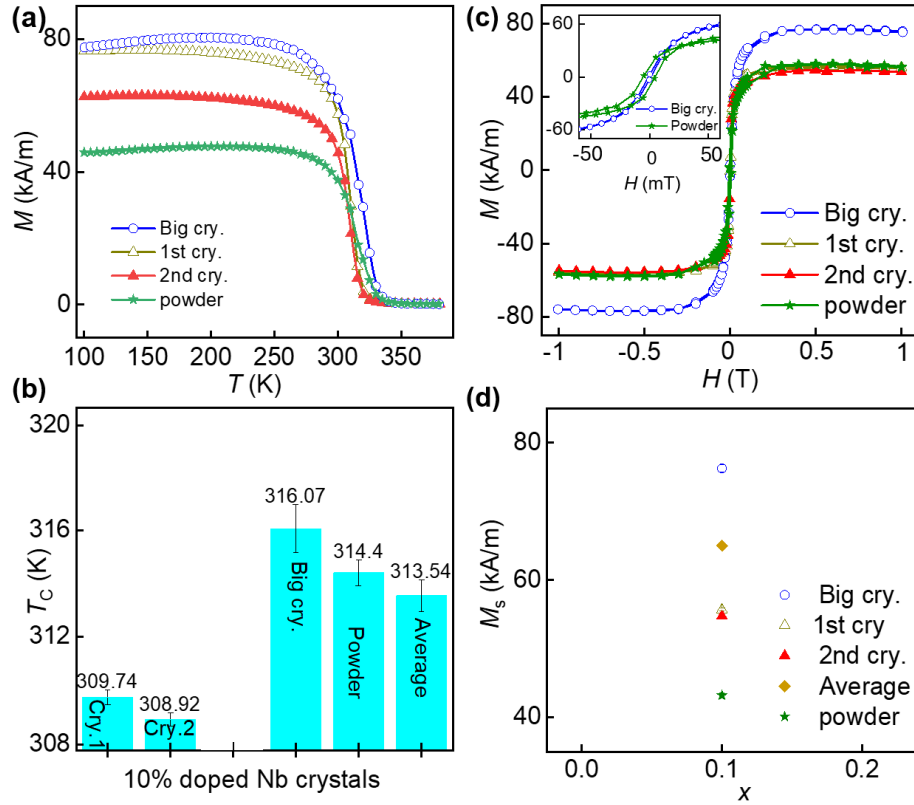


Figure S2.1. Magnetic measurements of 1T-Cr_{0.9}Nb_{0.1}Te₂ crystals. (a) In-plane magnetization (M) versus temperature (T) curves at a magnetic field of 30 mT, showing a ferromagnetic to paramagnetic transition in the range of 309 – 318 K. (b) In plane $M-H$ hysteresis loops measured at 300 K. Curie temperature T_c (c) and saturation magnetization M_s (d) as a function of Nb doping factor x .

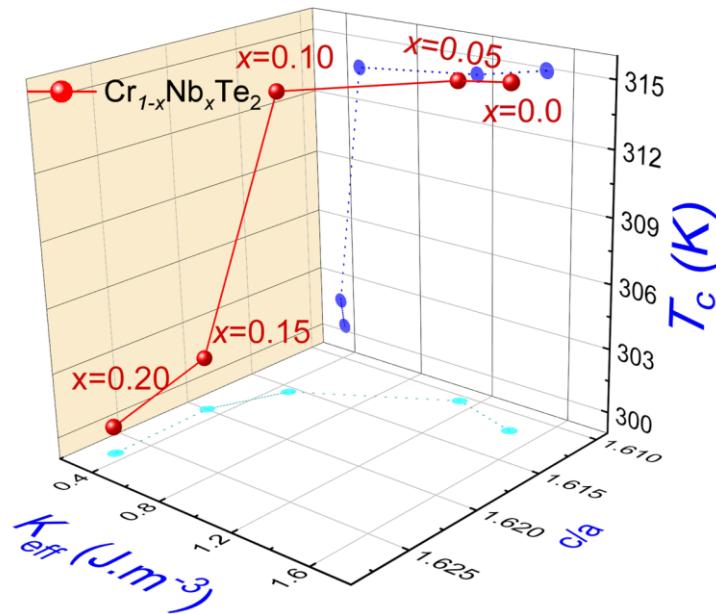


Figure S2.2. 3D representation of T_c , $\mu_0 H_A$, c/a ratio, and Nb doping.

Section S3: Density functional theory (DFT) calculations

The magnetic anisotropy energy of $1T\text{-Cr}_{1-x}\text{Nb}_x\text{Te}_2$ is obtained from the internal energy difference between the out-of-plane (E_{out} , Figure S3a) and in-plane (E_{in} , Figure S3b) spin configurations in the unit cell. The effective anisotropy coefficient K_{eff} is deduced as:

$$K_{\text{eff}} = \frac{E_{\text{out}} - E_{\text{in}}}{V_{\text{uc}}},$$

where V_{uc} is the unit cell volume.

The Curie temperature T_{C} was estimated within the mean-field approximation, where it relates to the Heisenberg exchange parameters as:^[59]

$$T_{\text{C}} = \frac{1}{3k_{\text{B}}} \sum J = \frac{1}{3k_{\text{B}}} (6J_{\parallel} + 2J_{\perp}),$$

where k_{B} is the Boltzmann constant, J_{\parallel} and J_{\perp} denote the in-plane and out-of-plane exchange interactions, respectively, as discussed and shown in Figure 6d in the main text. The calculated T_{C} values are plotted as function of the Nb doping factor x , see Figure S4c. For pristine $1T\text{-CrTe}_2$, the calculated T_{C} of 424 K exceeds the experimental value of 316 K (main text and Figure 2c). This change can be explained the overestimation of T_{C} using mean field theory,^[79] the 0 K-temperature calculated J_{\parallel} and J_{\perp} , and the presence of defects or oxidation effects of the $1T\text{-CrTe}_2$ crystals. With Nb doping, T_{C} decreases, primarily driven by the reduction of J_{\parallel} (see main text and Figure 6d).

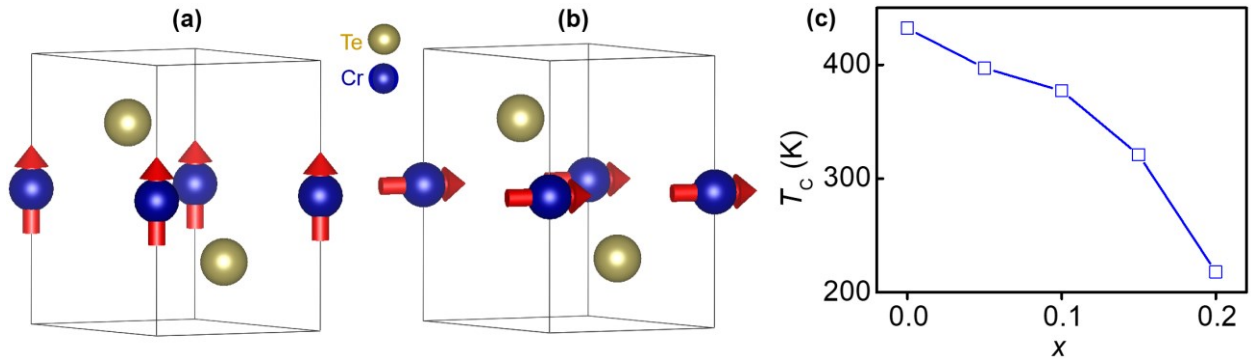


Figure S3. (a,b) Spin configurations of $\text{Cr}_{1-x}\text{Nb}_x\text{Te}_2$ used in the magnetic anisotropy calculations: (a) out-of-plane and (b) in-plane spin orientations. (c) Calculated Curie temperature T_{C} as a function of Nb concentration.

References

- [1] K. S. Burch, D. Mandrus, J.-G. Park, *Nature* **2018**, 563, 47.
- [2] M. Gibertini, M. Koperski, A. F. Morpurgo, K. S. Novoselov, *Nat. Nanotechnol.* **2019**, 14, 408.
- [3] B. Huang, G. Clark, E. Navarro-Moratalla, D. R. Klein, R. Cheng, K. L. Seyler, D. Zhong, E. Schmidgall, M. A. McGuire, D. H. Cobden, W. Yao, D. Xiao, P. Jarillo-Herrero, X. Xu, *Nature* **2017**, 546, 270.
- [4] C. Gong, L. Li, Z. Li, H. Ji, A. Stern, Y. Xia, T. Cao, W. Bao, C. Wang, Y. Wang, Z. Q. Qiu, R. J. Cava, S. G. Louie, J. Xia, X. Zhang, *Nature* **2017**, 546, 265.

- [5] W. Jin, Z. Ye, X. Luo, B. Yang, G. Ye, F. Yin, H. H. Kim, L. Rojas, S. Tian, Y. Fu, S. Yan, H. Lei, K. Sun, A. W. Tsen, R. He, L. Zhao, *PNAS* **2020**, *117*, 24664.
- [6] T. Song, Q.-C. Sun, E. Anderson, C. Wang, J. Qian, T. Taniguchi, K. Watanabe, M. A. McGuire, R. Stöhr, D. Xiao, T. Cao, J. Wrachtrup, X. Xu, *Science* **2021**, *374*, 1140.
- [7] S. Jiang, L. Li, Z. Wang, K. F. Mak, J. Shan, *Nature Nanotech* **2018**, *13*, 549.
- [8] S. Fu, K. Kang, K. Shayan, A. Yoshimura, S. Dadras, X. Wang, L. Zhang, S. Chen, N. Liu, A. Jindal, X. Li, A. N. Pasupathy, A. N. Vamivakas, V. Meunier, S. Strauf, E.-H. Yang, *Nat Commun* **2020**, *11*, 2034.
- [9] F. Zhang, B. Zheng, A. Sebastian, D. H. Olson, M. Liu, K. Fujisawa, Y. T. H. Pham, V. O. Jimenez, V. Kalappattil, L. Miao, T. Zhang, R. Pendurthi, Y. Lei, A. L. Elías, Y. Wang, N. Alem, P. E. Hopkins, S. Das, V. H. Crespi, M.-H. Phan, M. Terrones, *Advanced Science* **2020**, *7*, 2001174.
- [10] K. M. McCreary, A. G. Swartz, W. Han, J. Fabian, R. K. Kawakami, *Phys. Rev. Lett.* **2012**, *109*, 186604.
- [11] X. Hong, K. Zou, B. Wang, S.-H. Cheng, J. Zhu, *Phys. Rev. Lett.* **2012**, *108*, 226602.
- [12] B. Huang, M. A. McGuire, A. F. May, D. Xiao, P. Jarillo-Herrero, X. Xu, *Nat. Mater.* **2020**, *19*, 1276.
- [13] D. Zhong, K. L. Seyler, X. Linpeng, R. Cheng, N. Sivadas, B. Huang, E. Schmidgall, T. Taniguchi, K. Watanabe, M. A. McGuire, W. Yao, D. Xiao, K.-M. C. Fu, X. Xu, *Science Advances* **2017**, DOI 10.1126/sciadv.1603113.
- [14] W. Zhang, P. K. J. Wong, R. Zhu, A. T. S. Wee, *InfoMat* **2019**, *1*, 479.
- [15] L. Thiel, Z. Wang, M. A. Tschudin, D. Rohner, I. Gutiérrez-Lezama, N. Ubrig, M. Gibertini, E. Giannini, A. F. Morpurgo, P. Maletinsky, *Science* **2019**, *364*, 973.
- [16] D. A. Broadway, S. C. Scholten, C. Tan, N. Donschuk, S. E. Lillie, B. C. Johnson, G. Zheng, Z. Wang, A. R. Oganov, S. Tian, C. Li, H. Lei, L. Wang, L. C. L. Hollenberg, J.-P. Tetienne, *Advanced Materials* **2020**, *32*, 2003314.
- [17] A. Laraoui, K. Ambal, *Appl. Phys. Lett.* **2022**, *121*, 060502.
- [18] I. Fescenko, R. Kumar, T. Gas-Osoth, Y. Wang, S. Lamichhane, T. Li, A. Erickson, N. Raghavan, T. Delord, C. D. Cress, N. Proscia, S. W. LaGasse, S. Liou, X. Hong, J. J. Fonesca, T. An, C. A. Meriles, A. Laraoui, *Adv Funct Materials* **2025**, e12391.
- [19] M. Huang, J. Zhou, D. Chen, H. Lu, N. J. McLaughlin, S. Li, M. Alghamdi, D. Djugba, J. Shi, H. Wang, C. R. Du, *Nat Commun* **2022**, *13*, 5369.
- [20] A. J. Healey, S. C. Scholten, T. Yang, J. A. Scott, G. J. Abrahams, I. O. Robertson, X. F. Hou, Y. F. Guo, S. Rahman, Y. Lu, M. Kianinia, I. Aharonovich, J.-P. Tetienne, *Nat. Phys.* **2023**, *19*, 87.
- [21] L. Chen, J.-H. Chung, B. Gao, T. Chen, M. B. Stone, A. I. Kolesnikov, Q. Huang, P. Dai, *Phys. Rev. X* **2018**, *8*, 041028.
- [22] I. Lee, F. G. Utermohlen, D. Weber, K. Hwang, C. Zhang, J. van Tol, J. E. Goldberger, N. Trivedi, P. C. Hammel, *Phys. Rev. Lett.* **2020**, *124*, 017201.
- [23] L. N. Kapoor, S. Mandal, P. C. Adak, M. Patankar, S. Manni, A. Thamizhavel, M. M. Deshmukh, *Adv. Mater.* **2021**, *33*, 2005105.
- [24] A. McCreary, J. R. Simpson, T. T. Mai, R. D. McMichael, J. E. Douglas, N. Butch, C. Dennis, R. Valdés Aguilar, A. R. Hight Walker, *Phys. Rev. B* **2020**, *101*, 064416.
- [25] D. Lujan, J. Choe, M. Rodriguez-Vega, Z. Ye, A. Leonardo, T. N. Nunley, L.-J. Chang, S.-F. Lee, J. Yan, G. A. Fiete, R. He, X. Li, *Nat Commun* **2022**, *13*, 2527.

- [26] T. M. J. Cham, S. Karimeddiny, A. H. Dismukes, X. Roy, D. C. Ralph, Y. K. Luo, *Nano Lett.* **2022**, *22*, 6716.
- [27] L. Y. Shi, Y. Q. Liu, T. Lin, M. Y. Zhang, S. J. Zhang, L. Wang, Y. G. Shi, T. Dong, N. L. Wang, *Phys. Rev. B* **2018**, *98*, 094414.
- [28] H. Xu, K. Jia, Y. Huang, F. Meng, Q. Zhang, Y. Zhang, C. Cheng, G. Lan, J. Dong, J. Wei, J. Feng, C. He, Z. Yuan, M. Zhu, W. He, C. Wan, H. Wei, S. Wang, Q. Shao, L. Gu, M. Coey, Y. Shi, G. Zhang, X. Han, G. Yu, *Nat Commun* **2023**, *14*, 3824.
- [29] Y. Wang, J. Xia, H. Xu, G. Lan, X. Han, G. Yu, *Adv Funct Materials* **2025**, e17690.
- [30] Z.-N. 震南 Wang 王, Y.-P. 延培 Lv 吕, H.-N. 浩男 Chang 常, J. 俊 Zhang 张, *Chinese Phys. B* **2025**, *34*, 107201.
- [31] L. Qiu, Z. Wang, X.-S. Ni, D.-X. Yao, Y. Hou, *Applied Physics Letters* **2023**, *122*, 102402.
- [32] D. C. Freitas, R. Weht, A. Sulpice, G. Remenyi, P. Strobel, F. Gay, J. Marcus, M. Núñez-Regueiro, *J. Phys.: Condens. Matter* **2015**, *27*, 176002.
- [33] F. Fabre, A. Finco, A. Purbawati, A. Hadj-Azzem, N. Rougemaille, J. Coraux, I. Philip, V. Jacques, *Phys. Rev. Materials* **2021**, *5*, 034008.
- [34] X. Zhang, Q. Lu, W. Liu, W. Niu, J. Sun, J. Cook, M. Vaninger, P. F. Miceli, D. J. Singh, S.-W. Lian, T.-R. Chang, X. He, J. Du, L. He, R. Zhang, G. Bian, Y. Xu, *Nat Commun* **2021**, *12*, 2492.
- [35] L. Meng, Z. Zhou, M. Xu, S. Yang, K. Si, L. Liu, X. Wang, H. Jiang, B. Li, P. Qin, P. Zhang, J. Wang, Z. Liu, P. Tang, Y. Ye, W. Zhou, L. Bao, H.-J. Gao, Y. Gong, *Nat Commun* **2021**, *12*, 809.
- [36] G. Hu, B. Xiang, *Nanoscale Research Letters* **2020**, *15*, 226.
- [37] V. P. Ningrum, B. Liu, W. Wang, Y. Yin, Y. Cao, C. Zha, H. Xie, X. Jiang, Y. Sun, S. Qin, X. Chen, T. Qin, C. Zhu, L. Wang, W. Huang, *Research* **2020**, *2020*, DOI 10.34133/2020/1768918.
- [38] N. Abuawwad, M. D. S. Dias, H. Abusara, S. Lounis, *Phys. Rev. B* **2023**, *108*, 094409.
- [39] M. Yang, Q. Li, R. V. Chopdekar, R. Dhall, J. Turner, J. D. Carlström, C. Ophus, C. Klewe, P. Shafer, A. T. N'Diaye, J. W. Choi, G. Chen, Y. Z. Wu, C. Hwang, F. Wang, Z. Q. Qiu, *Sci. Adv.* **2020**, *6*, eabb5157.
- [40] L. Powalla, M. T. Birch, K. Litzius, S. Wintz, F. S. Yasin, L. A. Turnbull, F. Schulz, D. A. Mayoh, G. Balakrishnan, M. Weigand, X. Yu, K. Kern, G. Schütz, M. Burghard, *Advanced Materials* **2023**, *35*, 2208930.
- [41] A. Erickson, Q. Zhang, H. Vakili, C. Li, S. Sarin, S. Lamichhane, L. Jia, I. Fescenko, E. Schwartz, S.-H. Liou, J. E. Shield, G. Chai, A. A. Kovalev, J. Chen, A. Laraoui, *ACS Nano* **2024**, *18*, 31261.
- [42] A. Erickson, Q. Zhang, H. Vakili, E. Schwartz, S. Lamichhane, C. Li, B. Li, D. Song, G. Chai, S. Liou, A. A. Kovalev, J. Chen, A. Laraoui, *Small* **2025**, *21*, e05204.
- [43] A. V. Chumak, V. I. Vasyuchka, A. A. Serga, B. Hillebrands, *Nature Phys* **2015**, *11*, 453.
- [44] R. Timalina, B. Giri, H. Wang, A. Erickson, S. Sarin, S. Lamichhane, S. Liou, J. E. Shield, X. Xu, A. Laraoui, *Adv Elect Materials* **2024**, 2400398.
- [45] X. S. Wang, X. R. Wang, *Journal of Applied Physics* **2021**, *129*, 151101.
- [46] F. Zhuo, J. Kang, A. Manchon, Z. Cheng, *Advanced Physics Research* **2025**, *4*, 2300054.
- [47] D. D. Awschalom, C. R. Du, R. He, F. J. Heremans, A. Hoffmann, J. Hou, H. Kurebayashi, Y. Li, L. Liu, V. Novosad, J. Sklenar, S. E. Sullivan, D. Sun, H. Tang, V. Tyberkevych, C. Trevillian, A. W. Tsien, L. R. Weiss, W. Zhang, X. Zhang, L. Zhao, Ch. W. Zollitsch, *IEEE Trans. Quantum Eng.* **2021**, *2*, 1.

- [48] H. Y. Yuan, Y. Cao, A. Kamra, R. A. Duine, P. Yan, *Physics Reports* **2022**, *965*, 1.
- [49] D. Kikuchi, D. Prananto, K. Hayashi, A. Laraoui, N. Mizuochi, M. Hatano, E. Saitoh, Y. Kim, C. A. Meriles, T. An, *Appl. Phys. Express* **2017**, *10*, 103004.
- [50] M. Fukami, J. C. Marcks, D. R. Candido, L. R. Weiss, B. Soloway, S. E. Sullivan, N. Deegan, F. J. Heremans, M. E. Flatté, D. D. Awschalom, *Proc. Natl. Acad. Sci. U.S.A.* **2024**, *121*, e2313754120.
- [51] R. Timalisina, H. Wang, B. Giri, A. Erickson, X. Xu, A. Laraoui, *Adv Elect Materials* **2024**, *10*, 2300648.
- [52] A. Kumar, S. Dutta, S. Kim, T. Kwon, S. S. Patil, N. Kumari, S. Jeevanandham, I. S. Lee, *Chem. Rev.* **2022**, *122*, 12748.
- [53] Y. Liu, S. Kwon, G. J. De Coster, R. K. Lake, M. R. Neupane, *Phys. Rev. Materials* **2022**, *6*, 084004.
- [54] P. Gao, X. Li, J. Yang, *J. Phys. Chem. Lett.* **2021**, *12*, 6847.
- [55] S. A. Rincón-Ortiz, J. Rodríguez-Pereira, R. Ospina, *Surface Science Spectra* **2020**, *27*, 024014.
- [56] S. Lamichhane, R. Timalisina, C. Schultz, I. Fescenko, K. Ambal, S.-H. Liou, R. Y. Lai, A. Laraoui, *Nano Lett.* **2024**, *24*, 873.
- [57] A. Erickson, S. Q. A. Shah, A. Mahmood, P. Buragohain, I. Fescenko, A. Gruverman, C. Binek, A. Laraoui, *Adv Funct Materials* **2024**, *34*, 2408542.
- [58] X. Zhang, Y. Li, Q. Lu, X. Xiang, X. Sun, C. Tang, M. Mahdi, C. Conner, J. Cook, Y. Xiong, J. Inman, W. Jin, C. Liu, P. Cai, E. J. G. Santos, C. Phatak, W. Zhang, N. Gao, W. Niu, G. Bian, P. Li, D. Yu, S. Long, *Advanced Materials* **2024**, *36*, 2311591.
- [59] Charles Kittel, “Introduction to Solid State Physics, 8th Edition | Wiley,” can be found under <https://www.wiley.com/en-us/Introduction+to+Solid+State+Physics%2C+8th+Edition-p-9780471415268>, **2004**.
- [60] J.-M. L. Beaujour, A. D. Kent, D. W. Abraham, J. Z. Sun, *Journal of Applied Physics* **2008**, *103*, 07B519.
- [61] T. L. Gilbert, *IEEE Trans. Magn.* **2004**, *40*, 3443.
- [62] V. Unikandanunni, R. Medapalli, M. Asa, E. Albisetti, D. Petti, R. Bertacco, E. E. Fullerton, S. Bonetti, *Phys. Rev. Lett.* **2022**, *129*, 237201.
- [63] A. Laraoui, J. Vénuat, V. Halté, M. Albrecht, E. Beaurepaire, J.-Y. Bigot, *Journal of Applied Physics* **2007**, *101*, 09C105.
- [64] M. Dowran, A. Butler, S. Lamichhane, A. Erickson, U. Kilic, S. Liou, C. Argyropoulos, A. Laraoui, *Advanced Optical Materials* **2023**, 2300392.
- [65] M. Dowran, U. Kilic, S. Lamichhane, A. Erickson, J. Barker, M. Schubert, S. Liou, C. Argyropoulos, A. Laraoui, *Laser & Photonics Reviews* **2025**, *19*, 2400705.
- [66] A. S. Silva, S. P. Sá, S. A. Bunyaev, C. Garcia, I. J. Sola, G. N. Kakazei, H. Crespo, D. Navas, *Sci Rep* **2021**, *11*, 43.
- [67] T. Yu, S. Sharma, Y. M. Blanter, G. E. W. Bauer, *Phys. Rev. B* **2019**, *99*, 174402.
- [68] P. Giannozzi, S. Baroni, N. Bonini, M. Calandra, R. Car, C. Cavazzoni, D. Ceresoli, G. L. Chiarotti, M. Cococcioni, I. Dabo, A. Dal Corso, S. De Gironcoli, S. Fabris, G. Fratesi, R. Gebauer, U. Gerstmann, C. Gougoussis, A. Kokalj, M. Lazzeri, L. Martin-Samos, N. Marzari, F. Mauri, R. Mazzarello, S. Paolini, A. Pasquarello, L. Paulatto, C. Sbraccia, S. Scandolo, G. Sclauzero, A. P. Seitsonen, A. Smogunov, P. Umari, R. M. Wentzcovitch, *J. Phys.: Condens. Matter* **2009**, *21*, 395502.

- [69] M. J. Van Setten, M. Giantomassi, E. Bousquet, M. J. Verstraete, D. R. Hamann, X. Gonze, G.-M. Rignanese, *Computer Physics Communications* **2018**, 226, 39.
- [70] J. P. Perdew, K. Burke, M. Ernzerhof, *Phys. Rev. Lett.* **1996**, 77, 3865.
- [71] L. Bellaiche, D. Vanderbilt, *Phys. Rev. B* **2000**, 61, 7877.
- [72] H. Li, C. Li, B. Tao, S. Gu, Y. Xie, H. Wu, G. Zhang, G. Wang, W. Zhang, H. Chang, *Adv Funct Materials* **2021**, 31, 2010901.
- [73] Y. Deng, Y. Yu, Y. Song, J. Zhang, N. Z. Wang, Z. Sun, Y. Yi, Y. Z. Wu, S. Wu, J. Zhu, J. Wang, X. H. Chen, Y. Zhang, *Nature* **2018**, 563, 94.
- [74] W. Xing, L. Qiu, X. Wang, Y. Yao, Y. Ma, R. Cai, S. Jia, X. C. Xie, W. Han, *Phys. Rev. X* **2019**, 9, 011026.
- [75] E. A. Sanches, A. D. S. Carolino, A. L. D. Santos, E. G. R. Fernandes, D. M. Trichês, Y. P. Mascarenhas, *Advances in Materials Science and Engineering* **2015**, 2015, 1.
- [76] C. Zietlow, J. K. N. Lindner, *Ultramicroscopy* **2025**, 275, 114159.
- [77] L. H. F. Andrade, A. Laraoui, M. Vomir, D. Muller, J.-P. Stoquert, C. Estournès, E. Beaupaire, J.-Y. Bigot, *Phys. Rev. Lett.* **2006**, 97, 127401.
- [78] S. Yang, C. Feng, D. Spence, A. M. A. A. Al Hindawi, E. Latimer, A. M. Ellis, C. Binns, D. Peddis, S. S. Dhesi, L. Zhang, Y. Zhang, K. N. Trohidou, M. Vasilakaki, N. Ntallis, I. MacLaren, F. M. F. De Groot, *Advanced Materials* **2017**, 29, 1604277.
- [79] B. R. McGrath, R. E. Camley, K. L. Livesey, *Phys. Rev. B* **2020**, 101, 014444.